Cell

Multiparameter imaging reveals clinically relevant cancer cell-stroma interaction dynamics in head and neck cancer

Graphical abstract

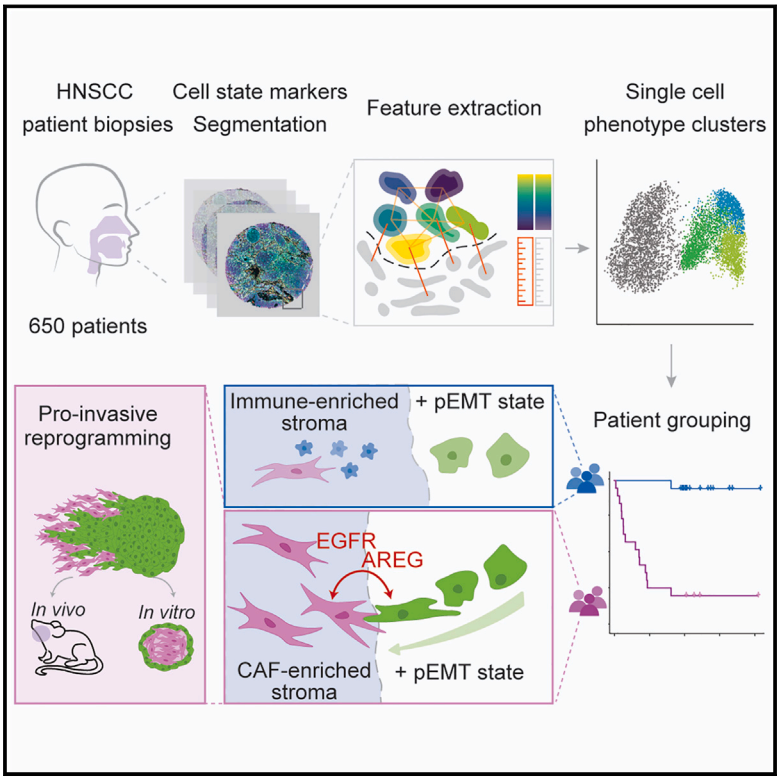

Highlights

- Integrative image analysis of cell state and morphology for cancer prognosis
- Combined tumor-stroma profiles generate clinically relevant phenotypic signatures
- Disease outcome of pEMT signature patients is highly sensitive to stromal composition
- pEMT state is required for pro-invasive reprogramming by cancer-associated fibroblasts

Authors

Karolina Punovuori, Fabien Bertillot, Yekaterina A. Miroshnikova, ..., Antti Mäkitie, Johanna Ivaska, Sara A. Wickström

Correspondence

sara.wickstrom@mpi-muenster.mpg.de

In brief

An image analysis pipeline that integrates cell-state and morphological markers identifies clinically relevant tumor phenotypes and cell-state-dependent interplay between tumor and stroma that drives cancer aggression.

Punovuori et al., 2024, Cell *187*, 1–18
December 12, 2024
https://doi.org/10.1016/j.cell.2024.09.046

CellPress

Cell

CellPress
OPEN ACCESS

Article

Multiparameter imaging reveals clinically relevant cancer cell-stroma interaction dynamics in head and neck cancer

Karolina Punovuori,[1] Fabien Bertillot,[1,2] Yekaterina A. Miroshnikova,[1,3] Mirjam I. Binner,[2] Satu-Marja Myllymäki,[1] Gautier Follain,[4] Kai Kruse,[5] Johannes Routila,[6] Teemu Huusko,[6] Teijo Pellinen,[7] Jaana Hagström,[8,9,10] Noemi Kedei,[11] Sami Ventelä,[6,4] Antti Mäkitie,[12,13,14] Johanna Ivaska,[4,15,16,17] and Sara A. Wickström[1,2,18,19,20,*]

[1]Stem Cells and Metabolism Research Program, Faculty of Medicine, University of Helsinki, 00290 Helsinki, Finland
[2]Department of Cell and Tissue Dynamics, Max Planck Institute for Molecular Biomedicine, 48149 Münster, Germany
[3]Laboratory of Molecular Biology, National Institute of Diabetes and Digestive and Kidney Diseases, National Institutes of Health, Bethesda, MD 20892, USA
[4]Turku Bioscience Centre, University of Turku and Åbo Akademi University, Turku, Finland
[5]Max Planck Institute for Molecular Biomedicine, 48149 Münster, Germany
[6]Department for Otorhinolaryngology, Head and Neck Surgery, University of Turku and Turku University Hospital, Kiinamyllynkatu 4-8, 20521 Turku, Finland
[7]Institute for Molecular Medicine Finland, Helsinki Institute of Life Science, University of Helsinki, Helsinki, Finland
[8]Department of Oral Pathology and Radiology, University of Turku, Turku University Hospital, Turku, Finland
[9]Research Programs Unit, Translational Cancer Medicine, University of Helsinki, Helsinki, Finland
[10]Department of Pathology, University of Helsinki, 00014 Helsinki, Finland
[11]Collaborative Protein Technology Resource, Office of Science and Technology, Center for Cancer Research, National Cancer Institute, Bethesda, MD 20892, USA
[12]Research Program in Systems Oncology, Faculty of Medicine, University of Helsinki, 00014 Helsinki, Finland
[13]Department of Otorhinolaryngology—Head and Neck Surgery, University of Helsinki and Helsinki University Hospital, HUS, 00029 Helsinki, Finland
[14]Division of Ear, Nose and Throat Diseases, Department of Clinical Sciences, Intervention and Technology, Karolinska Institute and Karolinska University Hospital, 17176 Stockholm, Sweden
[15]Department of Oncology and Radiotherapy, University of Turku and Turku University Hospital, Turku, Finland
[16]InFLAMES Research Flagship Center, University of Turku, Turku, Finland
[17]Foundation for the Finnish Cancer Institute, Tukholmankatu 8, 00014 Helsinki, Finland
[18]Helsinki Institute of Life Science, Biomedicum Helsinki, University of Helsinki, 00290 Helsinki, Finland
[19]Wihuri Research Institute, Biomedicum Helsinki, University of Helsinki, 00290 Helsinki, Finland
[20]Lead contact
*Correspondence: sara.wickstrom@mpi-muenster.mpg.de
https://doi.org/10.1016/j.cell.2024.09.046

SUMMARY

Epithelial tumors are characterized by abundant inter- and intra-tumor heterogeneity, which complicates diagnostics and treatment. The contribution of cancer-stroma interactions to this heterogeneity is poorly understood. Here, we report a paradigm to quantify phenotypic diversity in head and neck squamous cell carcinoma (HNSCC) with single-cell resolution. By combining cell-state markers with morphological features, we identify phenotypic signatures that correlate with clinical features, including metastasis and recurrence. Integration of tumor and stromal signatures reveals that partial epithelial-mesenchymal transition (pEMT) renders disease outcome highly sensitive to stromal composition, generating a strong prognostic and predictive signature. Spatial transcriptomics and subsequent analyses of cancer spheroid dynamics identify the cancer-associated fibroblast-pEMT axis as a nexus for intercompartmental signaling that reprograms pEMT cells into an invasive phenotype. Taken together, we establish a paradigm to identify clinically relevant tumor phenotypes and discover a cell-state-dependent interplay between stromal and epithelial compartments that drives cancer aggression.

Please cite this article in press as: Punovuori et al., Multiparameter imaging reveals clinically relevant cancer cell-stroma interaction dynamics in head and neck cancer, Cell (2024), https://doi.org/10.1016/j.cell.2024.09.046

INTRODUCTION

While decades of research have identified genomic drivers of cancer, most importantly oncogenic mutations and chromosomal abnormalities/rearrangements, it is less clear how architectural organization and spatial arrangement of the tumor and its microenvironment impact pathogenesis and how architecture is influenced by disease-associated cell states. In the absence of effective targeted therapies, surgery and (chemo)radiotherapy represent the primary treatment options for most cancers. However, these treatments are associated with significant morbidity due to side effects and, thus, a reduction in quality of life. Consequently, there is a clinical need for better molecular understanding of cancers and for development of prognostic indicators to aid decision making in respect of adjuvant treatment modalities.

Head and neck squamous cell carcinoma (HNSCC) is an aggressive, genetically complex, and difficult-to-treat group of cancers defined by their localization in the upper aerodigestive tract. The 5-year overall survival (OAS) rate remains at approximately 50%, the recurrence rate in HNSCC is about 50% during the first 2 years after diagnosis, and patients with failure after first-line therapy have a median OAS of less than 1 year.[1–3] Clinical-pathological parameters such as primary tumor site, nodal involvement, tumor thickness, and the status of the surgical margins have been shown to only weakly relate to prognosis, recurrence, survival, and treatment response.[4] Thus, there is a substantial unmet clinical need for improved diagnostics.

Partial epithelial-mesenchymal transition (pEMT) phenotypes have been identified in a number of tumor types, including HNSCC, and are associated with aggressive behavior and metastatic potential.[5–9] In addition to tumor-intrinsic properties, the tumor microenvironment also plays a key role in determining patient outcomes. For example, tumor-infiltrating lymphocytes (TILs) have been linked to improved survival in HNSCC,[10–12] and stromal microenvironments appear conserved across different cancer types and can correlate with clinical outcomes such as response to immunotherapy.[13,14] In particular, enhanced stromal fibrosis and stiffness have been shown to correlate with and drive cancer aggression.[15] However, how these stromal microenvironments interact with specific cancer cell states is unclear.

Here, we report a single-cell resolution image analysis pipeline that integrates morphological and spatial information with single-cell states using quantitative multiplex immunofluorescence. We combine biomarker profiles from the tumor and stroma to generate unique phenotypic signatures for single patients that are then grouped to compare clinical outcomes between patients with similar phenotypes. Our analysis reveals previously unreported subgroups of patients and, specifically, the combination of tumor pEMT status and cancer-associated fibroblast (CAF)-enriched fibrotic stroma as an indicator of poor survival. Using spatial transcriptomics, we identify highest signaling potential between these cell states through cancer-related extracellular matrix (onco-ECM) and epidermal growth factor (EGF) signaling pathways. Finally, using patient-derived cancer cell-CAF co-spheroids, we identify the pEMT state to be a pre-requisite for CAF-mediated reprogramming into an invasive phenotype through amphiregulin (AREG)/EGF signaling crosstalk. Collectively, these studies reveal the role of the cancer cell state in determining the impact of the stroma on disease aggression and outcome.

RESULTS

Multidimensional single-cell analysis reveals distinct tumor phenotypes in HNSCC

To identify clinically relevant cancer cell states, subpopulations, and architecture, we obtained pathologist-curated tumor microarrays (TMAs) containing samples from 212 HNSCC patients along with their full clinical information (Figure 1A). Samples consisted of primary (diagnostic) biopsies and, for a subset of patients, corresponding biopsies from post-radiotherapy tumors, lymph node metastases and recurrent tumors were included. Two serial sections were stained using multiplexed immunofluorescence to allow quantitative description of tissue architecture and cell states. The panel contained markers for cell and tissue morphology; epithelial, differentiation, and signaling states (keratins [K] 8 and 14, Epcam, and ß-catenin); stemness (Sox2, Bmi1, and K14); and pEMT (Slug and Vimentin), reported to be associated with aggressive cellular behaviors in HNSCC[8] (Figure 1B). Nuclei and cytoplasms were segmented and marker identities were quantified in the relevant subcellular compartments, along with parameters for nuclear shape and size (nuclear area, roundness, solidity, and elliptic Fourier coefficient [EFC] ratio[16]) and quantitative parameters of the local cellular neighborhood (local cell density/number of neighbors, distance from tumor-stroma interface, and alignment of cells relative to their neighbors). The analyses generated a multiparameter phenotypic descriptor for each single cell in the dataset.

All cells across all patients where then pooled, clustered using Louvain clustering,[17] and visualized using dimensional reduction with uniform manifold approximation and projection (UMAP)[18] (Figure S1A). This approach identified four major epithelial phenotype clusters within the dataset (Figures 1C–1E and S1A): a Sox2-high-K14-low population characterized by high cellular density (cluster 1); a K14-positive population of relatively large cells negative for both pEMT and stem cell markers, most commonly found centrally within tumors (cluster 2); a stem-cell-like cluster with high K14, Sox2, and Bmi1 (cluster 3); and a cluster with co-expression of K14, Slug, and Vimentin (cluster 0) (Figure 1D, inset). Together, these four phenotypes captured 89% of all the cells in the dataset; further clusters were also identified, but they corresponded to very rare cells present in only a few tumors (clusters 4+).

To explore the clinical relevance of these epithelial phenotypic clusters, we examined their relative abundance within each biopsy and grouped patients with similar cell composition using unsupervised Pearson's correlation-based hierarchical clustering (Figures 1F and S1B). Using this approach, we identified six "epithelial signatures," four of which could be defined by the dominance of a single phenotypic cluster. These signatures can be described as "dense Sox2-high K14-low," "stem-cell-enriched (Sox2/Bmi1-high K14-high)," "well differentiated," and "pEMT uniform" (groups B–E). The sixth signature (group F) consisted of a combination of three phenotypic clusters, whereas the samples in group A contained the internal control tissues ("healthy" liver) and a number of outlier tumors, collectively designated as a "mixed" signature. We subsequently projected

Please cite this article in press as: Punovuori et al., Multiparameter imaging reveals clinically relevant cancer cell-stroma interaction dynamics in head and neck cancer, Cell (2024), https://doi.org/10.1016/j.cell.2024.09.046

CellPress
OPEN ACCESS

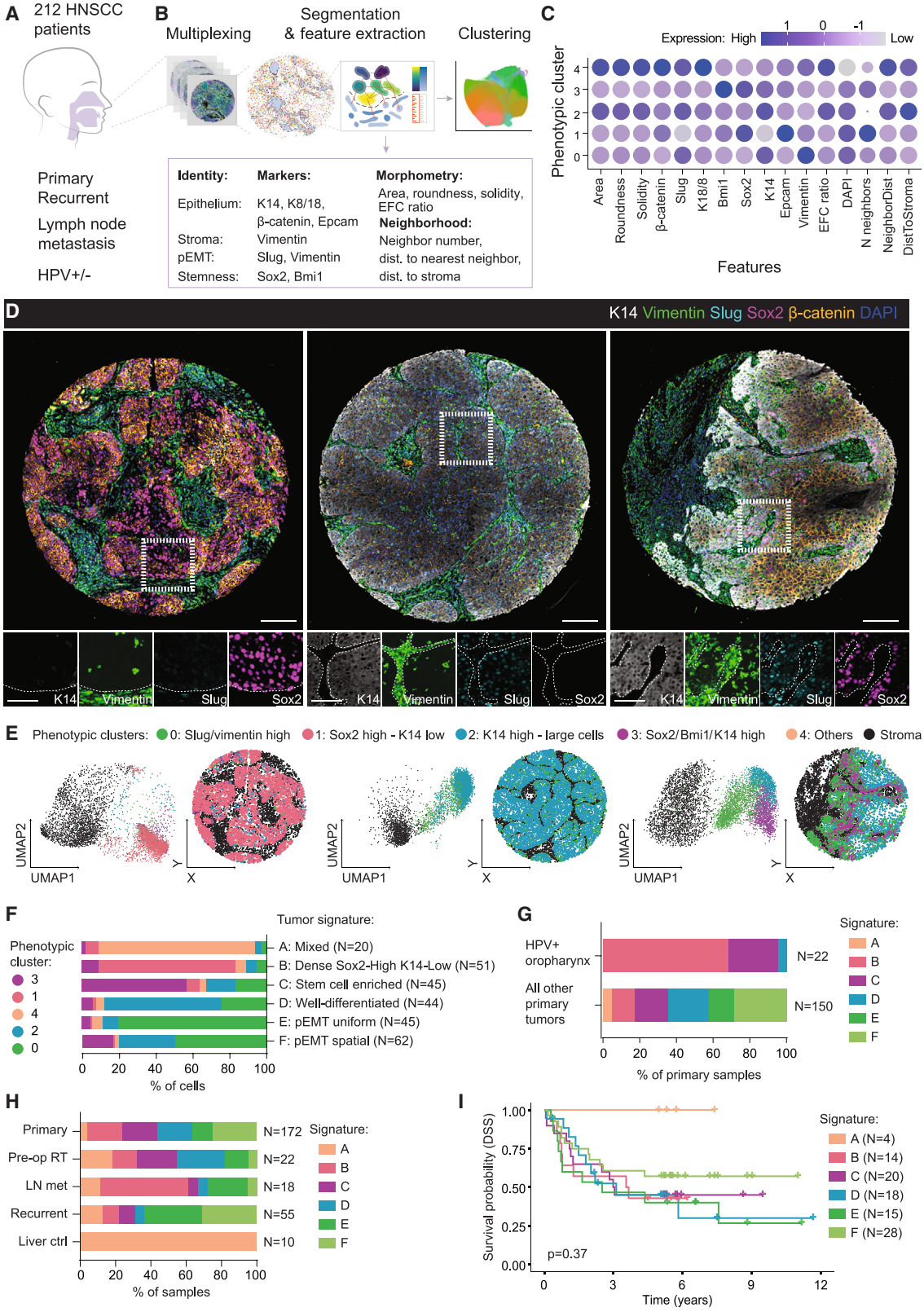

(legend on next page)

Please cite this article in press as: Punovuori et al., Multiparameter imaging reveals clinically relevant cancer cell-stroma interaction dynamics in head and neck cancer, Cell (2024), https://doi.org/10.1016/j.cell.2024.09.046

each cell back into XY space to study spatial distribution patterns of the phenotypic clusters (Figure S1C). In the case of F signature tumors, spatial analysis revealed that the pEMT (cluster 0) and Sox2-enriched (cluster 3) cell populations were found at the tumor-stroma interface, whereas the tumor cores were dominated by cells from the well-differentiated and K14-high phenotypic clusters (Figures S1C and S1D). We thus designated the F signature as "pEMT spatial."

Epithelial populations correlate with patient- and tumor-related parameters

Having identified six distinct epithelial signatures in HNSCC tumors, we next asked how these signatures correlate with histopathological/clinical features and disease outcomes. The 172 primary tumors represented a balanced mix of all six signatures (Figure 1F). Correlation analyses with clinical data (sex, alcohol consumption, and age at diagnosis) showed balanced distributions of patient signatures (Figure S1E). The two Sox2-high groups (groups B and C) were associated with the heaviest smokers and highest tumor staging (Figure S1E). Group B additionally contained the largest tumors (by T-stage) and highest status of lymph node metastasis (N-stage) (Figure S1E). Tumor grade varied widely between epithelial signatures: the K14-low tumors (groups A and B) were mostly poorly differentiated, whereas tumors with K14 expression and lack of stem-cell or EMT markers (group D) were mostly well differentiated (Figure S1E). One of the major clinically relevant disease subtypes within HNSCC is human papillomavirus (HPV)-positive oropharyngeal cancer, which is associated with specific treatment strategies, better outcomes than other HNSCCs,[19–21] and higher rates of lymph node metastasis,[22] which was confirmed in our dataset (Figure S1F). Strikingly, we found that 95% of all HPV+ oropharyngeal cancers fell into the two Sox2-high signatures (Figure 1G), indicating evolution of a specific phenotype in this disease. Because HPV+ oropharyngeal cancers represent a clinically distinct disease subtype, these samples were omitted from further analyses.

Importantly, no substantial differences in the frequencies of the epithelial signatures were observed in tumors originating from various anatomical sites, with the exception of the Sox2-enriched signature being absent from skin tumors and pEMT signatures being slightly enriched in the oral cavity tumors, indicating that anatomical variations in cell composition are unlikely to explain the different phenotypes (Figure S1G). By contrast, 50% of all lymph node metastases fell into the "dense Sox2-high K14-low" group, whereas over 60% of recurrent tumors were classified into one of the two pEMT signatures (Figure 1H). To understand whether a pEMT signature in the primary tumor could predict recurrence, we analyzed 5-year recurrence and lymph node metastasis in the primary tumor signature groups but found that prevalence of recurrence and metastasis were not substantially enriched in patients whose primary tumor had a pEMT signature compared with other groups (Figures S1H and S1I). Instead, when paired primary and recurrent tumors from the same patients were analyzed, we noted that a proportion of non-pEMT tumors "evolved" toward pEMT signatures upon recurrence (Figure S1J), providing a potential explanation for why the pEMT signature is more prevalent in recurring tumors.

Collectively, these analyses indicated that the patient signatures correlate well with histopathological grading and certain clinical risks factors. However, Kaplan-Meier analysis of primary tumors found no statistically significant difference in OAS or disease-specific survival (DSS) between the signatures (Figures 1I and S1K). To test whether the predictive power of any tumor phenotype was being masked in the survival analysis, we used Shapley additive explanations (SHAP) to examine local interaction effects between variables.[23] We computed the SHAP values of a Cox proportional hazards (CPHs) model trained on the OAS dataset. The analyses, together with additional survival analyses, showed that stage, recurrence, and age at diagnosis were predictors of disease outcome, whereas lymph node metastasis did not predict survival (Figures S1K–S1N). The predictive variables (age, sex, stage, or recurrence) did not significantly interact with pEMT signatures E and F (Figure S1N).

Collectively, these data indicated that by using a combination of cell-state markers and morphological features, we could generate epithelial tumor signatures that correlated with histopathological findings, were differentially abundant in progressed disease (metastasis and recurrence), and were able to differentiate disease type (HPV+ oropharynx) but did not strongly predict OAS in primary tumor biopsies.

Stromal composition is predictive of patient survival

As stromal subtypes have been shown to correlate with therapy responsiveness and patient outcomes across cancers,[13,14] we

Figure 1. Multidimensional single-cell analysis reveals distinct tumor phenotypes in HNSCC

(A) Overview of patient cohort.

(B) Quantified parameters and analysis workflow.

(C) Normalized expression of parameters across most abundant phenotypic clusters.

(D) Representative TMA images showing six merged channels. Scale bar, 150 μm. Dashed boxes denote magnified areas. Insets show selected single channels at higher magnification (scale bar, 75 μm). Dashed lines denote tumor/stroma border. Examples of Sox2-high/K14-low, well-differentiated, and pEMT spatial phenotypes are shown.

(E) Single cells from the three representative TMAs visualized using UMAP and spatial plots, with epithelial cells colored by their phenotypic cluster. Stromal cells are black.

(F) Distribution of epithelial phenotypic clusters across the tumor signatures. All primary and secondary samples and ten healthy liver controls are shown.

(G) Distribution of epithelial tumor signatures across HPV+ oropharynx and all other primary samples. HPV+ tumors fall into the Sox2-enriched signature.

(H) Distributions of epithelial tumor signatures across primary and secondary biopsies. Pre-op RT, samples from patients receiving pre-operative radiotherapy prior to their resection; LN met, lymph node metastases.

(I) Disease-specific survival across epithelial signatures; plot shows patients grouped based on primary biopsy. HPV+ oropharynx samples removed; log-rank test.

See also Figure S1.

Please cite this article in press as: Punovuori et al., Multiparameter imaging reveals clinically relevant cancer cell-stroma interaction dynamics in head and neck cancer, Cell (2024), https://doi.org/10.1016/j.cell.2024.09.046

CellPress
OPEN ACCESS

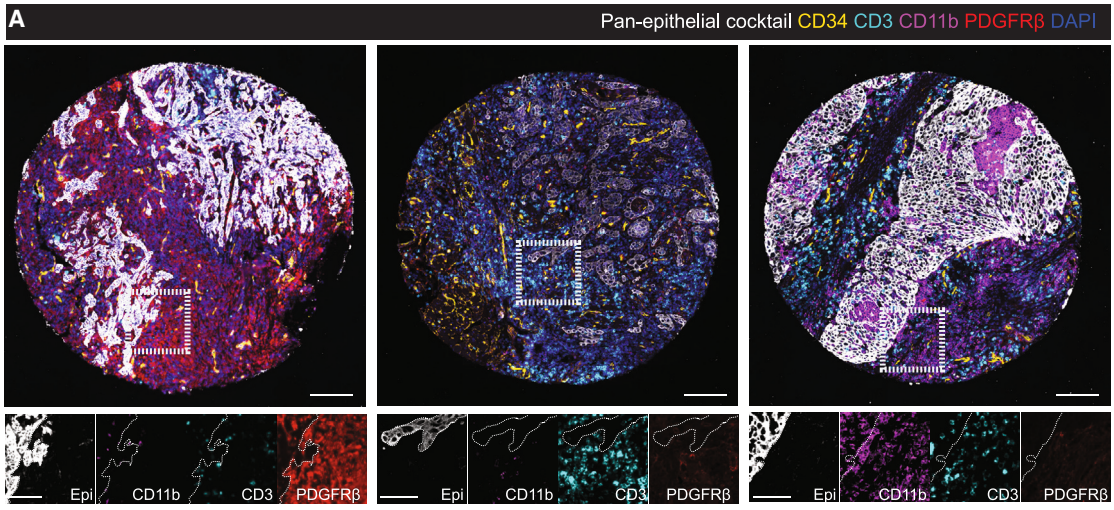

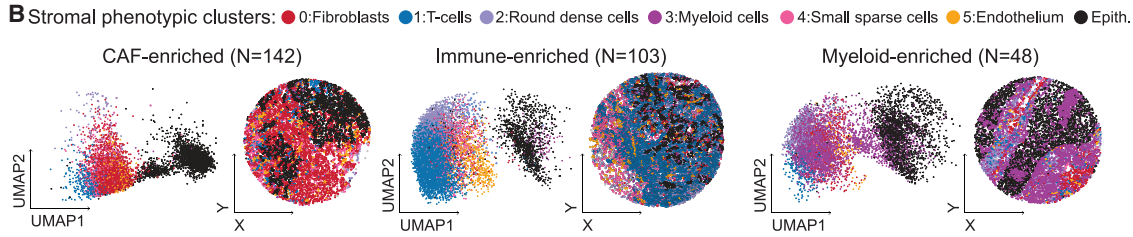

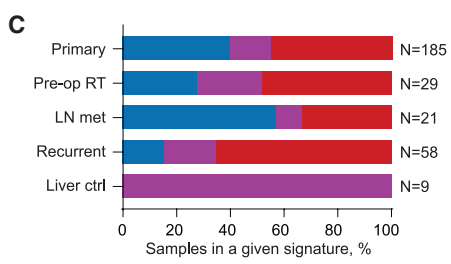

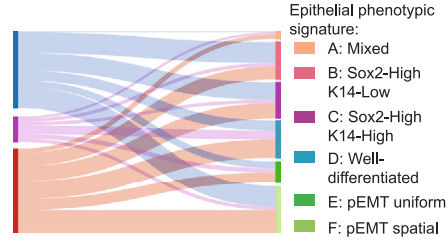

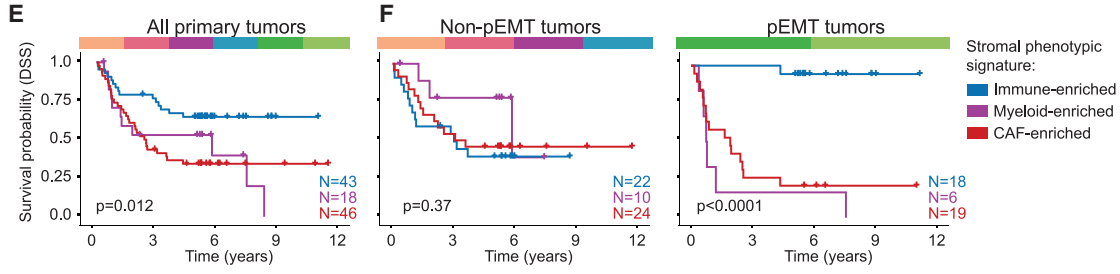

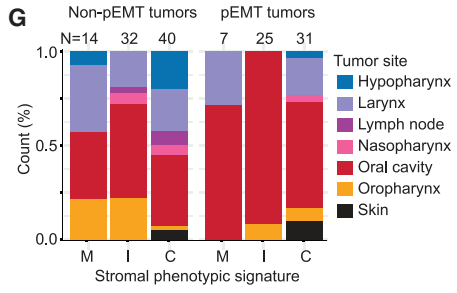

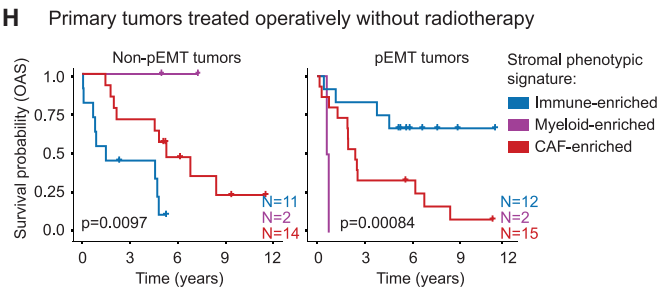

(legend on next page)

Please cite this article in press as: Punovuori et al., Multiparameter imaging reveals clinically relevant cancer cell-stroma interaction dynamics in head and neck cancer, Cell (2024), https://doi.org/10.1016/j.cell.2024.09.046

decided to extend the quantitative imaging strategy into the stromal compartment to better understand the stromal heterogeneity present in HNSCC. For analysis of stromal phenotypes, we used a marker panel to identify the predominant stromal cell types in the tumor microenvironment, including T cells and myeloid immune cells, vascular endothelium, and different classes of cancer-associated and normal fibroblasts (Figures 2A and S2A).

As expected, tumor stroma was found to contain a diversity of different cell types across the tumors analyzed (Figures 2A and 2B). Phenotypic clusters in the stroma had high correspondence with individual cell-type markers, allowing direct assignments of the dominant cell identities to the clusters (Figures S2B and S2C). We identified three major clusters based on dominant cell type: ''immune-enriched'' stroma (enriched for CD3+ cells and other small, densely packed cells), CAF-enriched fibrotic stroma (sparse, enriched for elongated and co-aligned cells expressing fibroblast markers), and myeloid-high stroma (enriched for cells expressing the myeloid marker CD11b) (Figures 2B and S2D).

As before, patients were then grouped based on similarity between their phenotypic clusters (Figure S2E). When primary and secondary tumor types were compared, the three stromal signatures were present across sample types, although immune signatures were more enriched in lymph node metastases, whereas recurrent tumors tended to present a CAF-enriched signature (Figure 2C). Interestingly, there was no cross-correlation between the epithelial and stromal patient signatures, and the six epithelial signatures were evenly distributed across the different stromal groups (Figure 2D).

Stromal signatures were found to be predictive of survival, with patients in the immune-enriched group having a five-year DSS of 64% compared with 34% for those with a CAF-enriched fibrotic stromal signature and 52% for those with a myeloid-enriched signature (Figure 2E). Collectively, in contrast to the epithelial phenotypes that correlated with clinical and histopathological features but did not strongly predict outcome, stromal phenotypic signatures are robust predictors of disease outcome independent of clinical and histopathological phenotypes (Figures 2E and S2F).

pEMT status and stromal signature combine into a highly predictive compound biomarker

Although the three stromal signatures did not correlate with specific epithelial signatures, we investigated whether combining the two signatures could increase predictive power and provide information on disease mechanisms. When patients from each epithelial group were separated by their stromal signature, a striking pattern emerged: in four out of six epithelial groups, survival was comparable across all stromal signatures, whereas in the two pEMT epithelial groups, stromal signatures revealed profound differences in survival outcomes (Figures S2G–S2L). When samples with the same responses were pooled together into larger patient groups for robust statistical analyses, there was no significant survival difference in patients with non-pEMT epithelial status, regardless of stromal signature (Figure 2E). By contrast, for patients with a pEMT epithelial signature, five-year DSS stood at 94% for those with an immune-enriched stroma compared with only 21% for those with a CAF-enriched stroma (Figure 2F). CPH modeling showed that out of prognostically relevant clinical parameters tested (tumor staging and grading), the pEMT/immune-high signature was the most significant predictor of positive outcomes in this patient population (Figure S2M).

To ensure that survival differences did not result from confounding effects caused by samples originating from distinct anatomical sites, we plotted the tumor site against the pEMT status of the epithelium and the phenotypic signature of the stroma (Figure 2G). Although minor differences in the proportion of different tumor sites in each group were present, an overall balanced representation of different primary tumor locations across the different signatures was observed, highlighting that the classification did not group patients based on gross tissue anatomy. Similarly, no confounding effects of different treatments were observed (Figure S2N).

Finally, we investigated whether the signatures could be used as predictive biomarkers, i.e., whether they could identify patient groups with good or poor responses to a specific treatment. For this purpose, we focused on patients in the dataset who had received only primary surgery (without adjuvant chemoradiotherapy). In this patient group, neither stromal nor epithelial

Figure 2. pEMT status and stromal signature combine into a highly predictive compound biomarker

(A) Representative TMA images of stromal marker panel stainings showing six merged channels. Scale bar, 150 μm. Dashed boxes denote magnified areas. Insets show selected single channels at higher magnification (scale bar, 75 μm). Dashed lines denote tumor/stroma border.

(B) Single cells from the representative TMA cores visualized using UMAP and spatial plots, with stromal cells colored by their phenotypic cluster identity. Epithelial cells are black.

(C) Distribution of stromal phenotypic signatures across different sample types; pre-op RT: samples from patients with pre-operative radiotherapy, LN met, lymph node metastases.

(D) Distribution of stromal phenotypic signatures within epithelial phenotypic signatures; stomal and epithelial signatures do not correlate.

(E) Disease-specific survival across the stromal phenotypic signatures; plot shows patients grouped based on primary biopsy; log-rank test. Stromal phenotypic signatures are predictive of survival.

(F) Disease-specific survival across stromal phenotypic signatures split by pEMT or non-pEMT epithelial phenotypic signature; log-rank test. Plots show patients grouped based on primary biopsy. Stromal phenotypic signatures have dramatically different survival in tumors with a pEMT signature. Samples with insufficient numbers of epithelial cells to assign to both signatures have been removed.

(G) Distribution of primary tumor sites across different stromal phenotypic signatures (M = myeloid-enriched; I = immune-enriched; C = CAF-enriched).

(H) Overall survival in patients treated with local operative treatment without additional radiotherapy; patients grouped based on the epithelial and stromal phenotypic signatures of primary biopsy; log-rank test. Combined epithelial/stromal signatures are predictive of survival in patients receiving the same treatment. HPV+ oropharynx samples removed in (E)–(H).

See also Figure S2.

Please cite this article in press as: Punovuori et al., Multiparameter imaging reveals clinically relevant cancer cell-stroma interaction dynamics in head and neck cancer, Cell (2024), https://doi.org/10.1016/j.cell.2024.09.046

CellPress
OPEN ACCESS

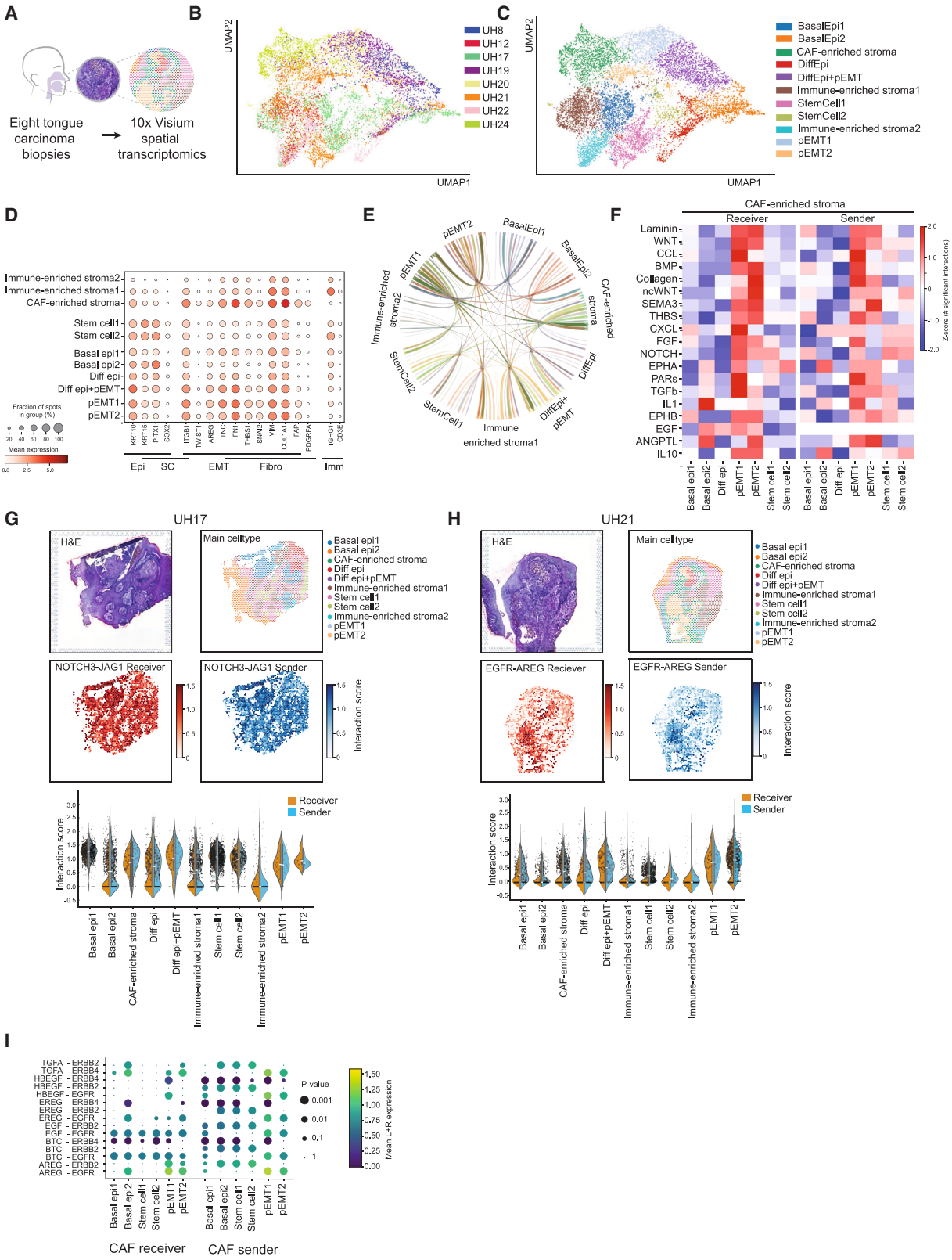

(legend on next page)

Please cite this article in press as: Punovuori et al., Multiparameter imaging reveals clinically relevant cancer cell-stroma interaction dynamics in head and neck cancer, Cell (2024), https://doi.org/10.1016/j.cell.2024.09.046

pEMT status alone were predictive of outcome (Figures S2O and S2P). By contrast, combining the two signatures was highly predictive: patients with a pEMT epithelial and immune-enriched stromal profile had significantly higher OAS compared with patients with the same epithelial status but a CAF-enriched stromal profile (Figure 2H). On the other hand, in non-pEMT tumors, this trend was reversed, indicating that profiling the stroma alone may be misleading for treatment selection, and suggesting complex biological interdependencies between epithelial and stromal phenotypes that influence tumor response to surgery.

Taken together, these results show that the combination of epithelial pEMT status and the immune cell/CAF balance of the stroma into a single tumor fingerprint forms an exceptionally strong biomarker of both treatment response and patient outcome in HNSCC tumors.

pEMT epithelium and CAF-enriched stroma represent a hub for intercompartment signaling

To understand why the combination of pEMT status and CAF-enriched stroma was predictive of poor survival, we sought to identify specific interactions between the distinct epithelial and stromal cell populations. To this end, we performed spatial transcriptomics (Visium platform, 10× Genomics) of an independent set of eight patient samples that were validated by immunofluorescence staining to represent the four major phenotypes observed previously: pEMT and non-pEMT epithelium, in combination with either immune-enriched or CAF-enriched stroma. To limit variation in gene expression arising from anatomical differences, all samples were from tongue squamous cell carcinoma (Figure 3A).

The samples were sequenced together, cell-cycle regressed, harmony integrated, and clustered together using Louvain clustering and projected in two dimensions (2D) using UMAP dimensional reduction (Figures 3B, 3C, and S3A). The resulting clusters were assigned biological identities based on a panel of selected marker genes and marker gene enrichment analyses (Figures 3D, S3B, and S3C). Importantly, the transcriptome-based clustering corresponded well with the initial classification of the tumors by immunofluorescence, with stem-cell-enriched, pEMT, and well-differentiated cancer clusters identified, as well as CAF- and immune-enriched stromal clusters (Figures 3C–3G and S3A–S3C). Enrichment analysis of terms in the Gene Ontology "biological processes" (GOBP) further indicated that whereas stem cell clusters were enriched for processes involving protein translation and keratinocyte differentiation, pEMT clusters were enriched for terms related to proliferation, migration, and ECM deposition (Figure S3D).

To infer putative signaling interactions between clusters, we quantified expression of matching ligand-receptor pairs (Figure 3E). Strikingly, the analysis consistently identified that stromal clusters enriched for a CAF-enriched signature were significantly more active in both outgoing and incoming signaling compared with immune-enriched stromal clusters across all patients. The same was true for epithelial clusters enriched for pEMT gene expression, which showed significantly more incoming and outgoing signaling activity compared with epithelial clusters with stem-cell-enriched, basal-like, or differentiated gene expression phenotypes (Figure 3E). The most enriched signaling pathways across patients and transcriptome clusters involved ECM ligand-receptor pairs with known pro-metastatic functions in cancer, including laminin, collagen, and thrombospondin pathways,[24] and the predicted interactions were strongest when occurring between pEMT cancer cells and CAF-enriched stroma (Figure 3F). In addition, known oncogenic signaling pathways, such as bone morphogenetic protein (BMP), Notch, fibroblast growth factor (FGF), and EGF, were enriched, again specifically between pEMT cancer cells and CAF-enriched stroma (Figure 3F). Some differences were also observed between immune-cell-enriched stroma and the epithelial states, where stem-cell-enriched areas showed enhanced predicted communication between interleukin 10 (IL-10) and Notch pathways, whereas pEMT states were enriched in IL-1 and transforming growth factor (TGF)-β signaling (Figure S3E).

We next focused on individual tumors to understand which of the signaling pathways are abundant in spatial proximity within their actual microenvironments and to identify the specific ligand-receptor pairs. To this end, we utilized COMMOT[25] to quantify spatial enrichment of tumors that contained pEMT, stem-cell-enriched and basal-like epithelial cells, and CAF- and immune-enriched stromal phenotypes. The most abundant spatial interactions were detected between *NOTCH3* and *JAG1*, which were enriched specifically between basal-like and stem-cell-enriched cancer cells and CAF-enriched stroma (Figure 3G). In contrast, the pEMT cancer cells showed the highest enrichment for receptor-ligand interactions between *AREG*, which encodes the protein AREG, a membrane-bound ligand of the EGF receptor (EGFR) as well as *EGFR* itself (Figures 3H and 3I).

Figure 3. pEMT epithelium and CAF-enriched stroma represent a hub for intercompartmental signaling

(A) Overview of spatial transcriptomics experimental design.

(B and C) UMAP plot of Harmony-integrated tumor spots with patient samples (B) or enriched phenotypic clusters (C) indicated.

(D) Dot plot of marker gene analyses for the enriched phenotype clusters. Dot size represents percentage of spots expressing marker and color the expression level.

(E) CellPhoneDB analysis of the number of predicted significant receptor-ligand interactions across enriched phenotypic clusters. Thickness of links is proportional to the interaction score. Note most abundant communication between pEMT-enriched and CAF-enriched clusters.

(F) Heatmap of top differential (*Z* score) predicted receptor-ligand interactions between the CAF-enriched cluster and indicated epithelial clusters.

(G and H) Spatial projections of enriched ligand-receptor interactions and their quantification across all phenotypic clusters in two representative patients indicate enhanced Notch3-Jag1 interactions between CAFs and stem-cell-enriched clusters (G) and EGFR-AREG interaction between CAFs and pEMT-enriched clusters (H).

(I) Dot plot of all identified EGF pathway ligand-receptor interaction between CAFs and epithelial phenotypes across three patients where all phenotypes are present (UH19, 20, 21).

See also Figure S3.

Please cite this article in press as: Punovuori et al., Multiparameter imaging reveals clinically relevant cancer cell-stroma interaction dynamics in head and neck cancer, Cell (2024), https://doi.org/10.1016/j.cell.2024.09.046

CellPress
OPEN ACCESS

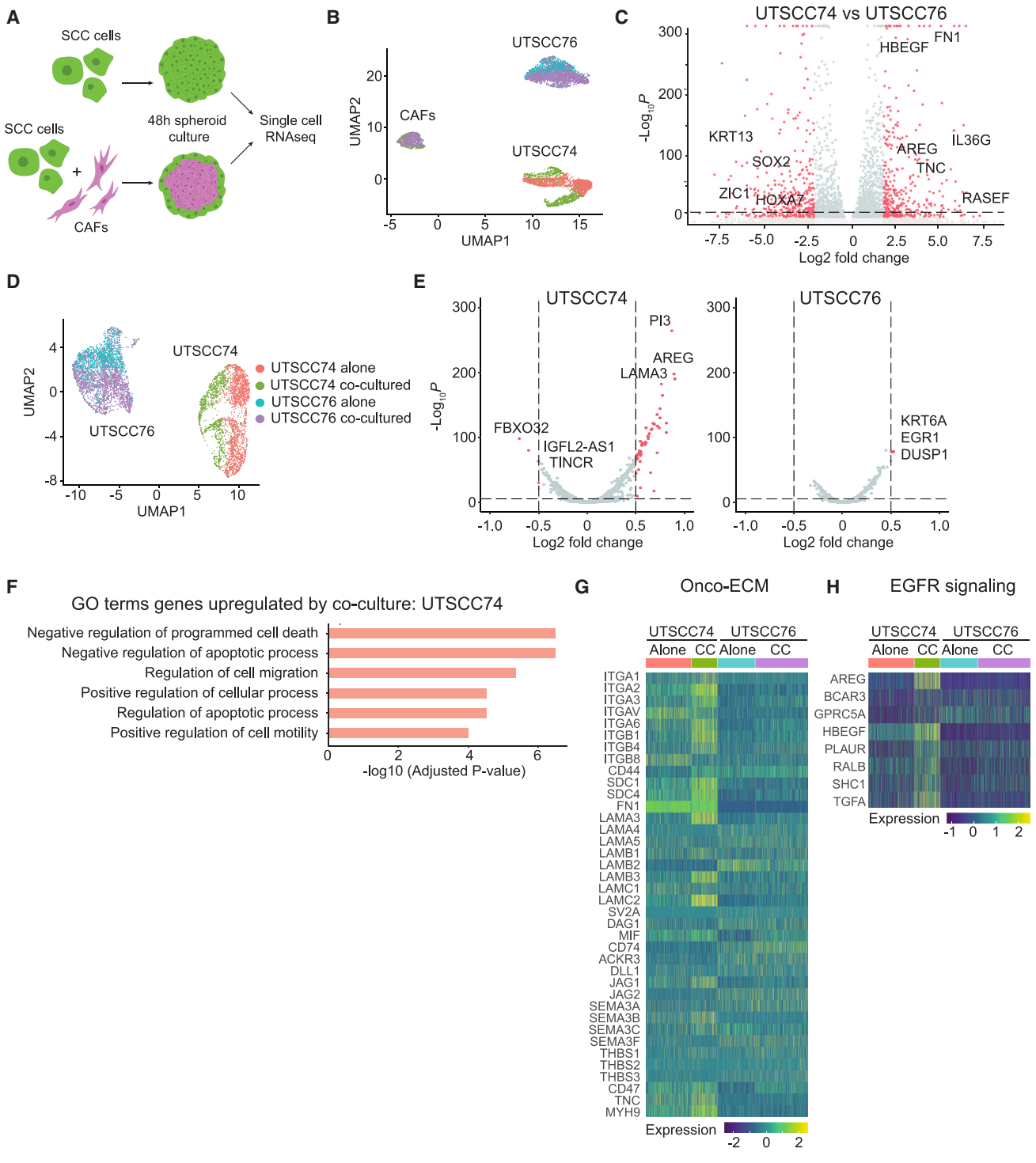

Figure 4. CAFs promote cell-state-specific reprogramming into a pro-invasive phenotype

(A) Experimental design of scRNA-seq.

(B) UMAP plot showing clustering of all cells analyzed by scRNA-seq.

(C) Differential gene expression analysis in two patient-derived cell lines. Relevant differentially expressed genes (< −0.5 or >0.5 $\log_2$ fold change) are labeled. Note high expression of stem cell genes such as *SOX2* in UTSCC76 and high expression of EMT-related ECM genes and *AREG* in UTSCC74.

(D) UMAP plot of cancer cells re-clustered without CAFs. Note separation of UTSCC74 clusters upon co-culture with CAFs.

(E) Differential gene expression analysis of the SCC cells upon co-culture with CAFs compared with the same cells cultured alone.

(F) GO terms enriched among genes upregulated in UTSCC74 cells co-cultured with CAFs compared with the same SCC cells cultured alone.

(legend continued on next page)

Please cite this article in press as: Punovuori et al., Multiparameter imaging reveals clinically relevant cancer cell-stroma interaction dynamics in head and neck cancer, Cell (2024), https://doi.org/10.1016/j.cell.2024.09.046

Taken together, these analyses confirmed that the tumor microenvironment is a significant source of signals to the cancer cells and identified the CAF-enriched stroma as having the strongest signaling output, owing mainly to large-scale signaling from the ECM. Intriguingly, the state of the tumor epithelium is key in determining whether these signals are received: tumor epithelia with pEMT-like gene expression are highly active in signaling with stroma through ECM and AREG-EGFR interactions, whereas tumor tissue with well-differentiated or stem-like states—or that are more centrally located within the tumors—have more limited signaling interactions with the tumor microenvironment and engage in signaling activity through ECM and Notch pathways.

CAFs promote cell-state-specific reprogramming into a pro-invasive phenotype

Having established the CAF-enriched stroma as a key source of signals transmitted specifically to the pEMT tumor cells, potentially through ECM and AREG-EGFR signaling, we next sought to characterize the precise nature and functional consequences of these signals. To this end, we established a three-dimensional (3D) spheroid co-culture model where patient-derived tongue cancer cells (UTSCC) were seeded into suspension cultures with or without patient-derived CAFs. The experiment was conducted in parallel on two different patient HNSCC lines co-cultured with the same CAF line. Within 24 h of seeding, the cells formed tight spheroids, both in mono- and co-culture conditions, and after 48 h cells were analyzed by single-cell RNA sequencing (scRNA-seq) (BD Rhapsody platform; Figure 4A).

Single-cell clustering showed that the three cell types separated well from each other, as expected (Figure 4B). We first examined gene expression differences in the cancer cell lines in the absence of CAF co-culture and found that EMT genes and components of EGFR signaling (*FN1*, *TNC*, *AREG*, and *HBEGF*) were significantly upregulated in UTSCC74 cells, whereas UTSCC76 showed upregulation of stem cell transcription factors (*SOX2*, *ZIC1*, and *GATA3*; Figures 4C and S4A; Table S1). Co-culture with CAFs resulted in separation of co-cultured HNSCC cells into their own cluster in the case of UTSCC74 but only to a limited extent in UTSCC76 cells (Figure 4D). This was confirmed by differential gene expression analysis, which showed significant up- and downregulation of 827 genes ($p$adj < 0.001) in the UTSCC74 cells following co-culture but only very few genes in the UTSCC76 cells (Figure 4E; Table S1). Interestingly, this result suggested that only the UTSCC74 cells mount a significant gene expression response to co-culture with CAFs.

To further probe which genetic programs defined the altered cell state in response to co-culture with CAFs, we performed GO-term analysis. The most significantly upregulated terms for UTSCC74 cells involved negative regulation of apoptosis and increased regulation of cell migration and motility (Figure 4F). By contrast, the terms upregulated in co-cultured UTSCC76 cells reflected metabolic alterations (Figure S4B). To understand why only the UTSCC74 cells showed pro-invasive reprogramming in response to co-culture, we investigated whether the EMT state was required for this response, as was predicted by the initial patient survival analyses. Comparing expression of a curated panel of EMT genes, we found that although both cell lines upregulated these genes in response to co-culture with CAFs, the baseline expression level and the subsequent transcriptional upregulation in response to co-culture were stronger in the UTSCC74 cells (Figures 4C and S4A). Interestingly, genes associated with the onco-ECM pathways most upregulated between CAF-enriched stroma and patient tumors in the *in vivo* spatial RNA-seq analysis were now strongly upregulated in the UTSCC74 cells in response to CAF co-culture, but not in UTSCC76 cells, suggesting that only the former are responsive to the onco-ECM signaling from the CAFs (Figure 4G).

We next asked whether a particular receptor on the UTSCC74 cells could be facilitating this specific responsiveness and interaction between the cancer cells and the CAFs. To this end, we turned to *AREG*, which was highly expressed in UTSCC74 cells compared with UTSCC76 cells, and, together with its counter receptor *EGFR*, also represented the most significantly enriched receptor-ligand interaction in the spatial transcriptomics dataset in the patient samples (Figures 4C, 3H, and 3I). Consistently, genes associated with EGFR signaling were upregulated in UTSCC74 cells in response to co-culture with CAFs, whereas UTSCC76 cells that had lower baseline *AREG* showed negligible upregulation of EGFR genes in response to co-culture (Figure 4H; Table S1). Finally, as the analyses in patient samples had indicated spatial proximity of CAFs and pEMT cells, and both AREG and EGFR are membrane bound, we next asked whether direct proximity of CAFs plays a role in the reprogramming of cancer cells by CAFs. Indeed, although direct co-culture of CAFs and UTSCC74 cells enhanced the expression of pEMT markers, conditioned medium of CAFs failed to do so (Figure S4C), indicating that close proximity of CAFs is required for efficient cancer cell reprogramming.

Taken together, the results suggested that not all cancer cells are equally susceptible to CAF-mediated signals and that a pre-existing pEMT state facilitates transcriptional reprogramming by CAFs. Further, interactions with pEMT cancer cells and CAFs are associated with increased EGFR signaling and correlated with *AREG* expression. This is in keeping with the observation that the pEMT-like state alone was not a predictor of negative outcomes in patients but additionally required the presence of a CAF-enriched stroma.

EMT state and CAF-mediated reprogramming are required to promote invasive behavior

To explore the functional consequences of CAF-mediated transcriptional reprogramming in cancer cells, we investigated the

(G) Changes in selected onco-ECM genes in patient-derived cancer cells cultured either alone or in co-culture (CC) with CAFs. UTSCC74, but not UTSCC76, cells upregulate onco-ECM genes in response to co-culture with CAFs.

(H) Changes in selected EGFR signaling pathway genes in cells cultured either alone or in co-culture with CAFs. UTSCC74, but not UTSCC76, cells upregulate EGFR signaling genes in response to co-culture (CC) with CAFs.

See also Figure S4.

Please cite this article in press as: Punovuori et al., Multiparameter imaging reveals clinically relevant cancer cell-stroma interaction dynamics in head and neck cancer, Cell (2024), https://doi.org/10.1016/j.cell.2024.09.046

CellPress
OPEN ACCESS

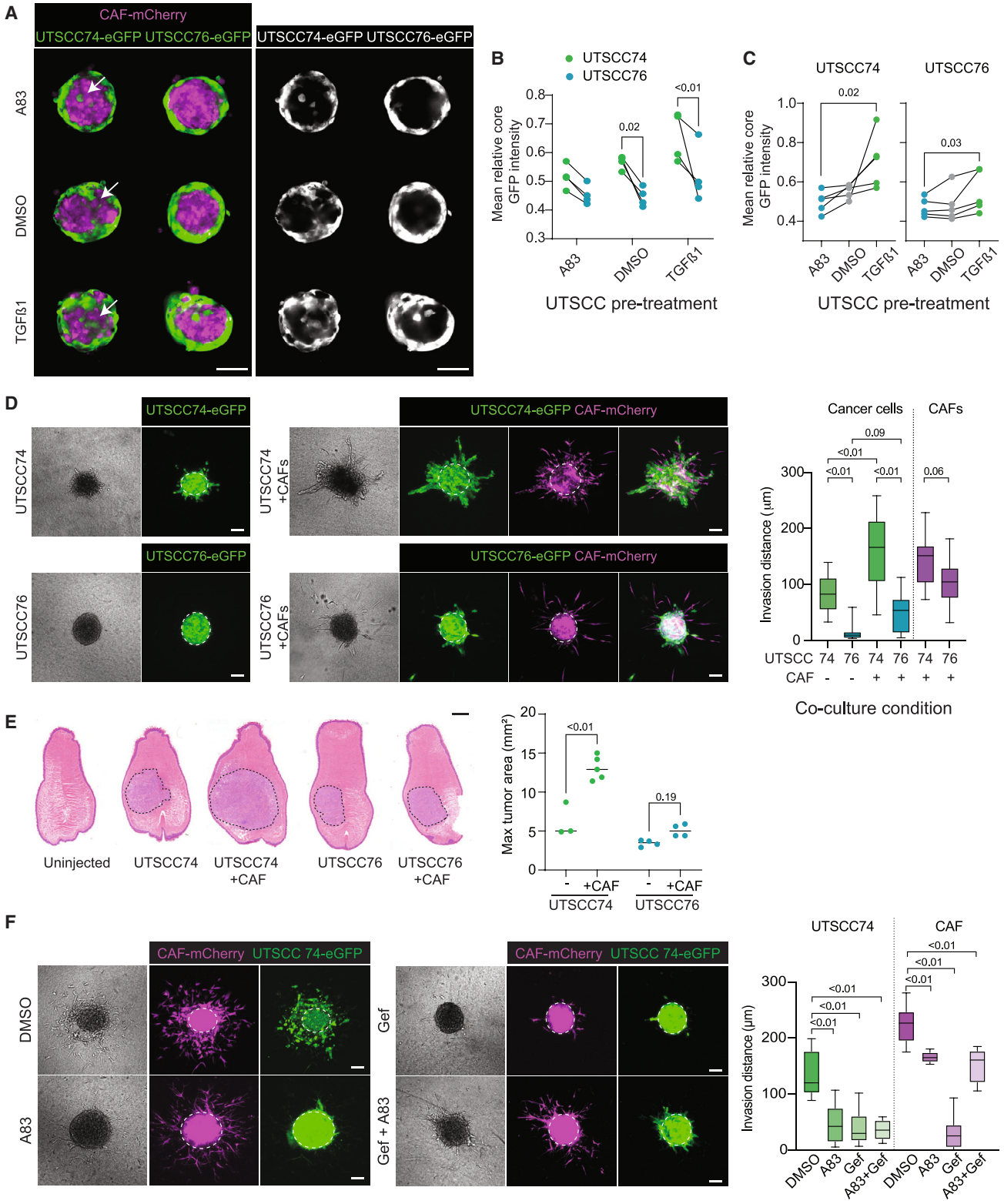

Figure 5. EMT state and CAF-mediated reprogramming are required to promote invasive behavior

(A) Representative images of UTSCC74-eGFP and -76a-eGFP cells pretreated with A83 or TGF-β1 for 72 h to prevent or promote EMT, imaged after 48 h of co-culture with CAF-mCherry cells. White arrows indicate CAF-HNSCC intermixing. Scale bar, 100 µm.

(legend continued on next page)

dynamics of UTSCC and CAF interactions and the role of the pEMT state in these dynamics. Within 48 h of seeding into co-culture, fluorescently tagged UTSCCs and CAFs formed spheroids with a stereotypic cell arrangement, with UTSCC cells forming an outer rim around a CAF core (Figure 5A). However, after 48 h of co-culture, UTSCC74 cells were capable of breaking the stereotypic cell arrangements and intermixed and infiltrated into the central CAF core. By contrast, UTSCC76 cells displayed significantly less intermixing behavior (Figures 5A–5C). However, this intermixing phenotype was observed in both UTSCC74 and -76 cells pretreated with the EMT-inducing growth factor TGF-β1[26] and could be inhibited by pre-treatment with the TGF-β inhibitor A83 (Figures 5A–5C).

To assay whether this dynamic intermixing behavior corresponded with productive invasiveness, we embedded the spheroids in 3D collagen. As predicted by the transcriptional signatures and the observed CAF-dependent reprogramming, UTSCC74 showed some invasion already in the absence of CAFs, and co-culture with CAFs substantially enhanced this behavior (Figure 5D). In contrast, UTSCC76 cells did not show invasive behavior in the absence or presence of CAFs (Figure 5D). To confirm that this difference was due to the difference in pEMT state of the cancer cells, we analyzed CAF-induced invasion in two additional patient-derived cell lines (one pEMT and one non-pEMT; Figures S5A and S5B) and observed that only the patient cell line with pEMT features responded to CAF co-culture with invasive behavior (Figure S5C). In contrast to the strong impact from the presence of CAFs, co-culture with healthy fibroblasts instead of CAFs resulted in the inability of the invasive UTSCC74 cancer cells to interact with the fibroblasts, assemble into spheroids, and co-invade (Figure S5D).

Importantly, this cell-state-dependent behavioral switch in response to CAFs was also observed *in vivo*: orthotopic transplantation of the cancer cells into the tongue tissue of mice showed that although there were no substantial differences between the *in vivo* expansion of patient-derived cell lines in the absence of CAFs, presence of CAFs greatly enhanced the expansion of UTSCC74 cells but had no impact on UTSCC76 growth (Figure 5E). Multiplexed immunofluorescence analysis and phenotypic clustering of cell states similar to the patient samples confirmed the presence of Sox2 stem-cell-enriched and pEMT-like cell states in the transplanted tumors (Figures S5E–S5G). As indicated by the *in vitro* and transcriptome analyses, the Sox2-high state was more abundant in UTSCC76 cells, whereas the UTSCC74 cells showed more abundant pEMT-like states (Figures S5F and S5G). Further, only the UTSCC74-cell-derived tumors responded to the presence of CAFs by relative expansion of the AREG-high pEMT-like states (Figures S5F and S5G).

To directly test the role of the pEMT state and AREG-EGFR signaling crosstalk between CAFs and cancer cells in pro-invasive behavior, we pretreated the UTSCC74 cells with a TGF-β1 inhibitor to attenuate pEMT and observed that this prevented cancer cell invasion but did not substantially impact the invasiveness of CAFs (Figure 5F). In contrast, treating co-cultures with the EGFR inhibitor Gefitinib blocked invasion of both cell types (Figure 5F). Intriguingly, pretreatment of the cancer cells with TGF-β1 inhibitor rendered CAFs insensitive to EGFR inhibition (Figure 5F), consistent with the observations from the sequencing analyses showing that the AREG-EGFR pathway is downstream of the pEMT state and that it acts bi-directionally between CAFs and pEMT cancer cells. Collectively, these results suggested that the CAF-mediated pro-invasive phenotype requires a pEMT state of cancer cells and is dependent on signaling through the EGFR receptor, potentially mediated by AREG.

pEMT state with pro-invasive signature associates with poor patient outcomes

Finally, to investigate whether the CAF-pEMT transcriptional reprogramming is relevant for HNSCC patient outcome, we proceeded to test this in clinical samples. We combined the previously applied tumor epithelium and stromal panels with identified molecular components of the CAF-HNSCC crosstalk and pro-invasive reprogramming, including components of the onco-ECM and associated mechanosignaling (Tenascin-C and Myh9) as well as AREG, and analyzed them in an additional, independent HNSCC patient cohort consisting of 438 primary tumors (Figures S6A–S6C). The resulting patient groups were consistent with those identified in the first cohort, were evenly distributed across anatomical sites (Figure S6D) and included stem-cell-enriched Sox2+/K14+, well-differentiated, pEMT-dominant, and pEMT spatial groups (Figure 6A). An additional Vimentin-enriched patient group was also identified (Figure S6E). Interestingly, including the additional markers to the epithelial staining panel improved the prognostic value of the epithelial signatures, with the mixed and EMT phenotypes showing poor

(B) Quantifications of intermixing (eGFP intensity in spheroid core to eGFP intensity at spheroid rim ratio) after 48 h of co-culture. Note that UTSCC74 cells display higher intermixing in all conditions and that TGF-β1 treatment enhances intermixing in both cell lines (n = 4 independent experiments with 3–7 spheroids/experiment; two-way ANOVA/Šídák's).

(C) Quantifications of intermixing after 48 h of co-culture (n = 4 independent experiments with 3–7 spheroids/experiment; repeat measures ANOVA/Tukey's).

(D) Representative images of UTSCC74-eGFP or UTSCC76-eGFP and CAF-mCherry spheroid invasion in 3D collagen. Dashed lines mark spheroid edges. Quantification shows average distance from spheroid edge, measured in four quadrants. Co-culture of CAFs with UTSCC74 cells triggers invasive behavior (n = 66 spheroids pooled across 3 independent experiments; one-way ANOVA/Tukey's). Scale bar, 100 μm.

(E) Representative H/E images and quantification of UTSCC74 and UTSCC76 cells orthotopically transplanted into mouse tongues with or without prior spheroid co-culture with CAFs. Note enhanced tumor expansion in UTSCC74+CAF condition (n = 3 mice [UTSCC74], 4 mice [UTSCC76, UTSCC76+CAF], and 5 mice [UTSCC74+CAF]; one-way ANOVA/Tukey's). Scale bar, 1 mm.

(F) Representative images and quantification of UTSCC74-eGFP and CAF-mCherry spheroid invasion in 3D collagen, where UTSCC74-eGFP were pretreated with A83 48 h prior to seeding into spheroids that were then treated with gefitinib (Gef) where indicated. Dashed lines mark spheroid edges. Note that A83 pre-treatment prevents cancer cell invasion and Gef blocks invasion of both cancer cells and CAFs. A83 pre-treatment renders CAFs insensitive to Gef (n = 34 spheroids pooled across 2 independent experiments; one-way ANOVA/Tukey's). Scale bar, 100 μm.

See also Figure S5.

Please cite this article in press as: Punovuori et al., Multiparameter imaging reveals clinically relevant cancer cell-stroma interaction dynamics in head and neck cancer, Cell (2024), https://doi.org/10.1016/j.cell.2024.09.046

CellPress
OPEN ACCESS

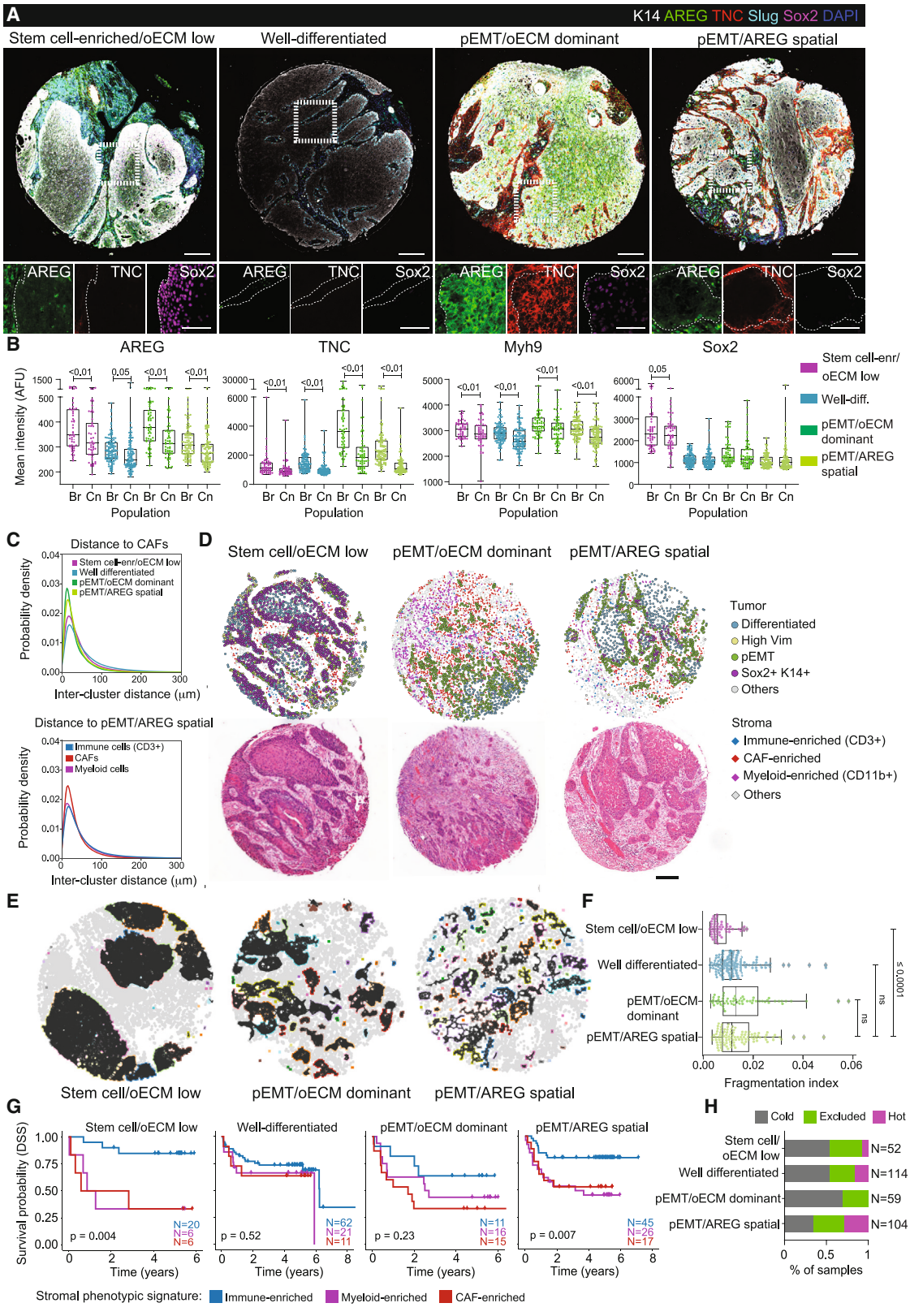

(legend on next page)

Please cite this article in press as: Punovuori et al., Multiparameter imaging reveals clinically relevant cancer cell-stroma interaction dynamics in head and neck cancer, Cell (2024), https://doi.org/10.1016/j.cell.2024.09.046

prognosis (Figure S6F). The stromal signature alone was also strongly predictive of survival (Figure S6G), as observed in the previous cohort.

Closer examination of the markers of CAF-HNSCC reprogramming showed that components of onco-ECM and AREG were enriched at the tumor-stroma boundary (Figure 6B), supporting their role as mediators of intercompartmental signaling. As predicted by the co-culture analyses, pEMT cells showed the strongest expression of the CAF-crosstalk markers (Figure 6B). To understand whether specific CAF subtypes were associated with these epithelial signatures, we further subclustered the CAFs based on their expression of FAP, αSMA, and PDGRFA into FAP-high/PDGFRA-high and αSMA-high clusters[27] but observed no specific enrichment (Figures S6H and S6I). Consistent with the notion of communication specifically between CAFs and pEMT cells, these two cell states showed the highest proximity among all tumor-stroma cell comparisons across patients (Figures 6C and 6D). In addition, analysis of tumor architecture revealed that the pEMT state was specifically associated with a fragmented architecture and loosely connected topological networks (Figures 6E and 6F), indicative of aggressive and potentially invasive behavior.

Importantly, the combined analysis of the stromal and epithelial panel further validated the strong prognostic value of the pEMT state-stromal identity combination, particularly when enriched at the tumor-stroma interface (pEMT spatial; Figure 6G). In addition, the stem-cell-enriched phenotypic group now showed a prognostic split between CAF-enriched stroma predicting poor outcome and immune-enriched stroma associating with favorable outcome (Figure 6G), albeit the patient numbers in this group were small and thus this result should be interpreted with caution. The stem-cell-enriched phenotype was also associated with enrichment of the crosstalk markers at the tumor-stroma interface (Figure 6B), consistent with previous studies showing relevance of Sox2-expressing cancer stem cells in SCC aggression.[28] Interestingly, although the pEMT-onco-ECM-dominant group still showed poor prognosis when combined with the CAF status of the stroma, the combined signature was no longer statistically significant in predicting survival. This effect could be due to the smaller patient group sizes but also linked to the loss of favorable survival prediction from the "immune-enriched stroma." To further investigate the prognostic value of the immune signature, we proceeded to analyze the localization of the immune cells within the patient samples. We classified patients according to their TIL status to "immune hot" and "immune cold" groups[29] (Figures S6J–S6L). Overall, the different TIL scores corresponded well with the immune-enriched stromal cluster and were evenly distributed across stromal and epithelial groups (Figures 6H and S6M). Interestingly, however, the pEMT uniform group was completely devoid of immune hot tumors and proportionally highest for immune cold tumors (Figure 6H). This indicated that the pEMT uniform state was associated with reduced levels of TILs, which are an independent indicator of favorable prognosis (Figure S6L), thus likely explaining the absence of a strong predictive signature of the stroma in this patient group.

Taken together, we conclude that the pEMT status of a tumor is predictive of its responsiveness to the surrounding stroma, with CAF-enriched fibrotic microenvironments combined with pEMT tumors resulting in the most aggressive cancer phenotypes. We further demonstrate that CAFs have the capacity to reprogram tumor cells into a pro-invasive phenotype but that this state is activated only in cells displaying some pre-existing propensity for a pEMT state. We propose that this interaction could be driven through EGFR and its ligand AREG, which are enriched in pEMT cells and drive dynamic interactions between these two cell types.

DISCUSSION

Understanding the mechanisms by which tumor heterogeneity and distinct cancer and stromal cell states drive cancer aggression is critical for improving diagnostic precision and development of targeted therapies. Here, using single-cell resolution quantitative image analysis combined with spatial transcriptomics, patient-derived spheroid cultures, and orthotopic transplants, we demonstrate that the combination of CAF-enriched stroma and epithelial pEMT status of the tumor serves as an exceptionally strong predictor of patient outcome and treatment response. We further observe that CAFs and pEMT cancer cells engage in dynamic signaling crosstalk that involves AREG-EGFR signaling to trigger cancer cell reprogramming into an invasive phenotype, providing a mechanistic explanation for the patient outcomes. Stromal composition has previously been identified as a strong predictor of patient outcome in a number of different cancers.[13,14] Likewise,

Figure 6. pEMT state with pro-invasive signature associates with worst patient outcomes

(A) Representative TMA images from four largest epithelial signature groups showing six merged channels. Scale bar, 150 μm. Dashed boxes denote magnified areas. Insets show selected single channels at higher magnification (scale bar, 75 μm); dashed lines denote tumor/stroma border. oECM, onco-ECM.

(B) Mean expression of selected markers in tumors from the four largest epithelial signature groups between tumor border (Br) and tumor center (Cn). Each dot represents the mean intensity of all cells within the given compartment in a single patient; paired t test. Note that markers of CAF-HNSCC crosstalk are enriched at tumor borders. AFU, arbitrary fluorescence units.

(C) Comparison of nearest distances between tumor cells and CAFs across epithelial signatures (top) and comparison of the nearest distances to tumor cells within the pEMT/AREG spatial epithelial signature across three main stroma clusters (bottom). Note that pEMT/AREG cells have the shortest distance to CAFs.

(D) Spatial projections of the main epithelial and stromal clusters (top) with corresponding H&E images (bottom).

(E) Representative topological neighborhood graphs of tumor sections from the three main epithelial signatures.

(F) Quantification of fragmentation index of tumors across the four main epithelial signatures. Minimum-to-maximum box plots show 75th, 50th, and 25th percentiles, each dot represents a single patient; ANOVA/Tukey's. Note fragmented architecture of pEMT tumors.

(G) Disease-specific survival across the four largest epithelial signature groups stratified by stromal composition; log-rank test.

(H) Tumor infiltrating lymphocyte/CD3 scoring in four major epithelial phenotypic signature groups. Note highest proportion of immune-cold and absence of immune-hot samples in pEMT/oECM dominant tumors.

See also Figure S6.

Please cite this article in press as: Punovuori et al., Multiparameter imaging reveals clinically relevant cancer cell-stroma interaction dynamics in head and neck cancer, Cell (2024), https://doi.org/10.1016/j.cell.2024.09.046

pEMT status of the tumor epithelium is emerging as an important biological program correlating with aggressive tumor behaviors in many cancers, including HNSCC.[5,8] Our study now shows that, in tumors with a pEMT epithelial signature, the composition of the stroma drastically affected patient outcomes, with patients with an immune-enriched stroma achieving five-year survival of 90% compared with just 21% in patients with the same epithelial profile but a CAF-enriched stroma. By contrast, tumors with a non-pEMT epithelial signature appeared to be largely agnostic to stromal composition.

Our cell communication analyses suggested that pEMT epithelia were more active in signaling with their surroundings than non-pEMT epithelia and that ECM signaling from CAF-enriched stroma in particular may drive aggressive behaviors in pEMT tumors. Although the functional analyses of patient-derived cells indicate that the presence of CAFs is sufficient to moderately enhance transcription of EMT-associated genes in cancer cells, the full invasive reprogramming involves EGFR signaling, most likely through AREG. This is consistent with the current view that EMT is a gradual transformation from a fully epithelial to a pEMT state that is associated with higher tumor grade, tumor relapse, and increased metastasis.[30–32] EGFR blockage combined with chemoradiotherapy is already the standard therapy for recurrent/metastatic HNSCC, and high expression of AREG is positively correlated with the efficacy of this treatment.[33] Interestingly, AREG has already been shown to mediated intrinsic pro-invasive crosstalk within CAFs[34]; our study now extends this mechanism to tumor-stroma crosstalk. The combined pEMT/CAF fingerprint—and, specifically, cancers with high AREG and onco-ECM expression—emerges as a cancer subtype with particularly poor treatment outcomes, suggesting that targeting fibroblast-pEMT crosstalk using EGFR inhibitors could be an effective candidate for a targeted therapy of these cancers. We further envision that the single-cell-resolution analyses developed here, which combines morphological and cell-state markers and provides additional biological information on the tumors, might be a useful diagnostic tool for HNSCC and other solid tumors.

Limitations of this study

The patient cohorts for the signature analyses are from biobank samples and represent retrospective analyses of patient outcome. Although this enables high throughput analyses of large patient cohorts, future prospective studies are needed to validate the predictive nature of the compound biomarkers. Further, although the spatial transcriptomics facilitated unbiased transcriptome-wide sampling of patient samples to establish hypotheses on tumor stroma communication validated in functional assays, this analysis lacks single-cell resolution, and although the clusters are enriched for the annotated cell types, the sequenced spots contain a mixture of various cell types. This precludes more detailed analysis of transcriptional profiles of the various cell types.

RESOURCE AVAILABILITY

Lead contact

Further information and requests for resources and reagents should be directed to and will be fulfilled by the lead contact, Sara A. Wickström (sara.wickstrom@mpi-muenster.mpg.de).

Materials availability

All unique/stable reagents generated in this study are available from the lead contact without restriction.

Data and code availability

- The RNA sequencing datasets are available at GEO: GSE251902,GSE252265.
- Analysis scripts and code are available at WickstromLab GitHub.
- Any additional information required to re-analyze data reported in this paper is available from the lead contact upon request.

ACKNOWLEDGMENTS

We thank Franziska Peters, Hanne Ahola, and Manuela Haustein for help with experiments; Blanca Majem for advice on transplantation experiments; Elisa Piccinini for patient sample collection; Annabrita Schoonenberg, Anette Holmström, and Antti Hassinen from the Institute for Molecular Medicine Finland (FIMM); the Max Planck Institute sequencing core facility; histology core facility of the Institute of Biomedicine, University of Turku; and Institute for Molecular Medicine Finland FIMM Genomics Unit for support with experiments. This work was supported by the Orion Foundation (to K.P. and Y.A.M.), Research Council of Finland (332402) and Turku Collegium for Science Medicine and Technologies postdoctoral grants (to G.F.), the Finnish Cancer Institute (to S.A.W. and K. Albin Johansson Professorship to J.I.), Academy of Finland Center of Excellence BarrierForce (#346131 to J.I. and S.A.W.), Academy of Finland Molecular Regulatory Networks of Life (#330033, NucleoMech; to A.M., J.I., and S.A.W.), and the Sigrid Juselius Foundation, Helsinki Institute of Life Science, Wihuri Research Institute, Business Finland R2B, and the Max Planck Society (all to S.A.W.).

AUTHOR CONTRIBUTIONS

K.P. designed and performed experiments, analyzed data, and co-developed the image analysis pipeline. F.B. co-developed the image analysis pipeline and analyzed data. Y.A.M. co-developed the image analysis pipeline, performed experiments, and analyzed data. M.I.B. performed invasion assays. S.-M.M. and G.F. performed transplantation assays. K.K. analyzed sequencing data. J.R., T.H., and S.V. generated the TMAs. T.P. provided advice on multiplexing and the imaging resource. J.H., S.V., and A.M. provided advice on clinical aspects of the study. N.K. performed multiplex imaging of tumor transplants. A.M. provided fresh tumor samples. J.I. provided cell lines, conceptual advice, and supervised transplantation assays. S.A.W. conceived the study and image analysis pipeline, designed experiments, and analyzed data. K.P. and S.A.W. wrote the manuscript with input from all authors.

DECLARATION OF INTERESTS

K.P., F.B., Y.A.M., and S.A.W. are listed as inventors on a patent application related to this work, filed through the technology transfer office of the University of Helsinki, with UoH being the patent applicant.

STAR★METHODS

Detailed methods are provided in the online version of this paper and include the following:

- KEY RESOURCES TABLE
- EXPERIMENTAL MODEL AND STUDY PARTICIPANT DETAILS
  - Patient samples
  - Cancer cell lines
- METHOD DETAILS
  - Patient samples
  - Multiplexed fluorescent immunohistochemical staining and imaging
  - Automated image analysis pipeline for processing large multiplexed TMA datasets
  - Single-cell clustering of cell phenotypes
  - Tumor architecture analyses

- Survival analysis
- Spatial transcriptomics
- Cancer cell / CAF 3D co-spheroids
- Imaging and image analysis
- Single-cell RNA sequencing and analysis
- 3D invasion
- In vivo orthotopic transplantation

- QUANTIFICATION AND STATISTICAL ANALYSIS

SUPPLEMENTAL INFORMATION

Supplemental information can be found online at https://doi.org/10.1016/j.cell.2024.09.046.

Received: January 16, 2024
Revised: July 25, 2024
Accepted: September 27, 2024
Published: October 28, 2024

REFERENCES

1. Alsahafi, E., Begg, K., Amelio, I., Raulf, N., Lucarelli, P., Sauter, T., and Tavassoli, M. (2019). Clinical update on head and neck cancer: molecular biology and ongoing challenges. Cell Death Dis. *10*, 540. https://doi.org/10.1038/s41419-019-1769-9.
2. Argiris, A., Karamouzis, M.V., Raben, D., and Ferris, R.L. (2008). Head and neck cancer. Lancet *371*, 1695–1709.
3. Bossi, P., Alfieri, S., Strojan, P., Takes, R.P., López, F., Mäkitie, A., Saba, N.F., Rodrigo, J.P., Bradford, C.R., Suarez, C., et al. (2019). Prognostic and predictive factors in recurrent and/or metastatic head and neck squamous cell carcinoma: A review of the literature. Crit. Rev. Oncol. Hematol. *137*, 84–91.
4. Jerjes, W., Upile, T., Petrie, A., Riskalla, A., Hamdoon, Z., Vourvachis, M., Karavidas, K., Jay, A., Sandison, A., Thomas, G.J., et al. (2010). Clinicopathological parameters, recurrence, locoregional and distant metastasis in 115 T1-T2 oral squamous cell carcinoma patients. Head Neck Oncol. *2*, 9. https://doi.org/10.1186/1758-3284-2-9.
5. Simeonov, K.P., Byrns, C.N., Clark, M.L., Norgard, R.J., Martin, B., Stanger, B.Z., Shendure, J., McKenna, A., and Lengner, C.J. (2021). Single-cell lineage tracing of metastatic cancer reveals selection of hybrid EMT states. Cancer Cell *39*, 1150–1162.e9. https://doi.org/10.1016/j.ccell.2021.05.005.
6. Wouters, J., Kalender-Atak, Z., Minnoye, L., Spanier, K.I., De Waegeneer, M., Bravo González-Blas, C., Mauduit, D., Davie, K., Hulselmans, G., Najem, A., et al. (2020). Robust gene expression programs underlie recurrent cell states and phenotype switching in melanoma. Nat. Cell Biol. *22*, 986–998. https://doi.org/10.1038/s41556-020-0547-3.
7. Vegliante, R., Pastushenko, I., and Blanpain, C. (2022). Deciphering functional tumor states at single-cell resolution. EMBO J. *41*, e109221. https://doi.org/10.15252/embj.2021109221.
8. Puram, S.V., Tirosh, I., Parikh, A.S., Patel, A.P., Yizhak, K., Gillespie, S., Rodman, C., Luo, C.L., Mroz, E.A., Emerick, K.S., et al. (2017). Single-Cell Transcriptomic Analysis of Primary and Metastatic Tumor Ecosystems in Head and Neck Cancer. Cell *171*, 1611–1624.e24. https://doi.org/10.1016/j.cell.2017.10.044.
9. Zhao, J., Guo, C., Xiong, F., Yu, J., Ge, J., Wang, H., Liao, Q., Zhou, Y., Gong, Q., Xiang, B., et al. (2020). Single cell RNA-seq reveals the landscape of tumor and infiltrating immune cells in nasopharyngeal carcinoma. Cancer Lett. *477*, 131–143. https://doi.org/10.1016/j.canlet.2020.02.010.
10. Nordfors, C., Grün, N., Tertipis, N., Ährlund-Richter, A., Haeggblom, L., Sivars, L., Du, J., Nyberg, T., Marklund, L., Munck-Wikland, E., et al. (2013). CD8+ and CD4+ tumour infiltrating lymphocytes in relation to human papillomavirus status and clinical outcome in tonsillar and base of tongue squamous cell carcinoma. Eur. J. Cancer *49*, 2522–2530. https://doi.org/10.1016/j.ejca.2013.03.019.
11. de Ruiter, E.J., Ooft, M.L., Devriese, L.A., and Willems, S.M. (2017). The prognostic role of tumor infiltrating T-lymphocytes in squamous cell carcinoma of the head and neck: A systematic review and meta-analysis. Oncoimmunology *6*, e1356148. https://doi.org/10.1080/2162402X.2017.1356148.
12. So, Y.K., Byeon, S.J., Ku, B.M., Ko, Y.H., Ahn, M.J., Son, Y.I., and Chung, M.K. (2020). An increase of CD8(+) T cell infiltration following recurrence is a good prognosticator in HNSCC. Sci. Rep. *10*, 20059. https://doi.org/10.1038/s41598-020-77036-8.
13. Bagaev, A., Kotlov, N., Nomie, K., Svekolkin, V., Gafurov, A., Isaeva, O., Osokin, N., Kozlov, I., Frenkel, F., Gancharova, O., et al. (2021). Conserved pan-cancer microenvironment subtypes predict response to immunotherapy. Cancer Cell *39*, 845–865.e7. https://doi.org/10.1016/j.ccell.2021.04.014.
14. Luo, H., Xia, X., Huang, L.B., An, H., Cao, M., Kim, G.D., Chen, H.N., Zhang, W.H., Shu, Y., Kong, X., et al. (2022). Pan-cancer single-cell analysis reveals the heterogeneity and plasticity of cancer-associated fibroblasts in the tumor microenvironment. Nat. Commun. *13*, 6619. https://doi.org/10.1038/s41467-022-34395-2.
15. Metcalf, K.J., Alazzeh, A., Werb, Z., and Weaver, V.M. (2021). Leveraging microenvironmental synthetic lethalities to treat cancer. J. Clin. Invest. *131*, e143765. https://doi.org/10.1172/JCI143765.
16. Tamashunas, A.C., Tocco, V.J., Matthews, J., Zhang, Q., Atanasova, K.R., Paschall, L., Pathak, S., Ratnayake, R., Stephens, A.D., Luesch, H., et al. (2020). High-throughput gene screen reveals modulators of nuclear shape. Mol. Biol. Cell *31*, 1392–1402. https://doi.org/10.1091/mbc.E19-09-0520.
17. Traag, V.A., Waltman, L., and van Eck, N.J. (2019). From Louvain to Leiden: guaranteeing well-connected communities. Sci. Rep. *9*, 5233. https://doi.org/10.1038/s41598-019-41695-z.
18. McInnes, L., Healy, J., and Melville, J. (2018). UMAP: Uniform Manifold Approximation and Projection for Dimension Reduction. Preprint at arXiv. https://doi.org/10.48550/arXiv.1802.03426.
19. Lindquist, D., Romanitan, M., Hammarstedt, L., Näsman, A., Dahlstrand, H., Lindholm, J., Onelöv, L., Ramqvist, T., Ye, W., Munck-Wikland, E., and Dalianis, T. (2007). Human papillomavirus is a favourable prognostic factor in tonsillar cancer and its oncogenic role is supported by the expression of E6 and E7. Mol. Oncol. *1*, 350–355. https://doi.org/10.1016/j.molonc.2007.08.005.
20. Fakhry, C., Westra, W.H., Li, S., Cmelak, A., Ridge, J.A., Pinto, H., Forastiere, A., and Gillison, M.L. (2008). Improved survival of patients with human papillomavirus-positive head and neck squamous cell carcinoma in a prospective clinical trial. J. Natl. Cancer Inst. *100*, 261–269. https://doi.org/10.1093/jnci/djn011.
21. Weinberger, P.M., Yu, Z., Haffty, B.G., Kowalski, D., Harigopal, M., Brandsma, J., Sasaki, C., Joe, J., Camp, R.L., Rimm, D.L., and Psyrri, A. (2006). Molecular classification identifies a subset of human papillomavirus–associated oropharyngeal cancers with favorable prognosis. J. Clin. Oncol. *24*, 736–747. https://doi.org/10.1200/JCO.2004.00.3335.
22. Bauwens, L., Baltres, A., Fiani, D.J., Zrounba, P., Buiret, G., Fleury, B., Benzerdjeb, N., and Grégoire, V. (2021). Prevalence and distribution of cervical lymph node metastases in HPV-positive and HPV-negative oropharyngeal squamous cell carcinoma. Radiother. Oncol. *157*, 122–129. https://doi.org/10.1016/j.radonc.2021.01.028.
23. Lundberg, S.M., Erion, G., Chen, H., DeGrave, A., Prutkin, J.M., Nair, B., Katz, R., Himmelfarb, J., Bansal, N., and Lee, S.I. (2020). From Local Explanations to Global Understanding with Explainable AI for Trees. Nat. Mach. Intell. *2*, 56–67. https://doi.org/10.1038/s42256-019-0138-9.
24. Kai, F., Drain, A.P., and Weaver, V.M. (2019). The Extracellular Matrix Modulates the Metastatic Journey. Dev. Cell *49*, 332–346. https://doi.org/10.1016/j.devcel.2019.03.026.
25. Cang, Z., Zhao, Y., Almet, A.A., Stabell, A., Ramos, R., Plikus, M.V., Atwood, S.X., and Nie, Q. (2023). Screening cell-cell communication in spatial transcriptomics via collective optimal transport. Nat. Methods *20*, 218–228. https://doi.org/10.1038/s41592-022-01728-4.

26. Xu, J., Lamouille, S., and Derynck, R. (2009). TGF-beta-induced epithelial to mesenchymal transition. Cell Res. *19*, 156–172. https://doi.org/10.1038/cr.2009.5.

27. Chhabra, Y., and Weeraratna, A.T. (2023). Fibroblasts in cancer: Unity in heterogeneity. Cell *186*, 1580–1609. https://doi.org/10.1016/j.cell.2023.03.016.

28. Boumahdi, S., Driessens, G., Lapouge, G., Rorive, S., Nassar, D., Le Mercier, M., Delatte, B., Caauwe, A., Lenglez, S., Nkusi, E., et al. (2014). SOX2 controls tumour initiation and cancer stem-cell functions in squamous-cell carcinoma. Nature *511*, 246–250. https://doi.org/10.1038/nature13305.

29. Mandal, R., Şenbabaoğlu, Y., Desrichard, A., Havel, J.J., Dalin, M.G., Riaz, N., Lee, K.W., Ganly, I., Hakimi, A.A., Chan, T.A., and Morris, L.G. (2016). The head and neck cancer immune landscape and its immunotherapeutic implications. JCI Insight *1*, e89829. https://doi.org/10.1172/jci.insight.89829.

30. Dongre, A., and Weinberg, R.A. (2019). New insights into the mechanisms of epithelial-mesenchymal transition and implications for cancer. Nat. Rev. Mol. Cell Biol. *20*, 69–84. https://doi.org/10.1038/s41580-018-0080-4.

31. Yang, J., Antin, P., Berx, G., Blanpain, C., Brabletz, T., Bronner, M., Campbell, K., Cano, A., Casanova, J., Christofori, G., et al. (2020). Guidelines and definitions for research on epithelial-mesenchymal transition. Nat. Rev. Mol. Cell Biol. *21*, 341–352. https://doi.org/10.1038/s41580-020-0237-9.

32. Zhang, Y., and Weinberg, R.A. (2018). Epithelial-to-mesenchymal transition in cancer: complexity and opportunities. Front. Med. *12*, 361–373. https://doi.org/10.1007/s11684-018-0656-6.

33. Kogashiwa, Y., Inoue, H., Kuba, K., Araki, R., Yasuda, M., Nakahira, M., and Sugasawa, M. (2018). Prognostic role of epiregulin/amphiregulin expression in recurrent/metastatic head and neck cancer treated with cetuximab. Head Neck *40*, 2424–2431. https://doi.org/10.1002/hed.25353.

34. Mucciolo, G., Araos Henríquez, J., Jihad, M., Pinto Teles, S., Manansala, J.S., Li, W., Ashworth, S., Lloyd, E.G., Cheng, P.S.W., Luo, W., et al. (2024). EGFR-activated myofibroblasts promote metastasis of pancreatic cancer. Cancer Cell *42*, 101–118.e11. https://doi.org/10.1016/j.ccell.2023.12.002.

35. Routila, J., Leivo, I., Minn, H., Westermarck, J., and Ventelä, S. (2021). Evaluation of prognostic biomarkers in a population-validated Finnish HNSCC patient cohort. Eur. Arch. Otorhinolaryngol. *278*, 4575–4585. https://doi.org/10.1007/s00405-021-06650-7.

36. Mylly, M., Nissi, L., Huusko, T., Routila, J., Vaittinen, S., Irjala, H., Leivo, I., and Ventelä, S. (2022). Epidemiological Study of p16 Incidence in Head and Neck Squamous Cell Carcinoma 2005-2015 in a Representative Northern European Population. Cancers (Basel) *14*, 5717. https://doi.org/10.3390/cancers14225717.

37. Routila, J., Suvila, K., Grénman, R., Leivo, I., Westermarck, J., and Ventelä, S. (2021). Cancer cell line microarray as a novel screening method for identification of radioresistance biomarkers in head and neck squamous cell carcinoma. BMC Cancer *21*, 868. https://doi.org/10.1186/s12885-021-08618-6.

38. Kaukonen, R., Mai, A., Georgiadou, M., Saari, M., De Franceschi, N., Betz, T., Sihto, H., Ventelä, S., Elo, L., Jokitalo, E., et al. (2016). Normal stroma suppresses cancer cell proliferation via mechanosensitive regulation of JMJD1a-mediated transcription. Nat. Commun. *7*, 12237. https://doi.org/10.1038/ncomms12237.

39. Virshup, I., Rybakov, S., Theis, F.J., Angerer, P., and Wolf, F.A. (2021). anndata: Annotated data. Preprint at bioRxiv. https://doi.org/10.1101/2021.12.16.473007.

40. Efremova, M., Vento-Tormo, M., Teichmann, S.A., and Vento-Tormo, R. (2020). CellPhoneDB: inferring cell-cell communication from combined expression of multi-subunit ligand-receptor complexes. Nat. Protoc. *15*, 1484–1506. https://doi.org/10.1038/s41596-020-0292-x.

41. Stirling, D.R., Swain-Bowden, M.J., Lucas, A.M., Carpenter, A.E., Cimini, B.A., and Goodman, A. (2021). CellProfiler 4: improvements in speed, utility and usability. BMC Bioinformatics *22*, 433. https://doi.org/10.1186/s12859-021-04344-9.

42. Chen, S. (2023). Ultrafast one-pass FASTQ data preprocessing, quality control, and deduplication using fastp. Imeta *2*, e107. https://doi.org/10.1002/imt2.107.

43. Korsunsky, I., Millard, N., Fan, J., Slowikowski, K., Zhang, F., Wei, K., Baglaenko, Y., Brenner, M., Loh, P.R., and Raychaudhuri, S. (2019). Fast, sensitive and accurate integration of single-cell data with Harmony. Nat. Methods *16*, 1289–1296. https://doi.org/10.1038/s41592-019-0619-0.

44. Berg, S., Kutra, D., Kroeger, T., Straehle, C.N., Kausler, B.X., Haubold, C., Schiegg, M., Ales, J., Beier, T., Rudy, M., et al. (2019). ilastik: interactive machine learning for (bio)image analysis. Nat. Methods *16*, 1226–1232. https://doi.org/10.1038/s41592-019-0582-9.

45. Blondel, V.D., Guillaume, J.-L., Lambiotte, R., and Lefebvre, E. (2008). Fast unfolding of communities in large networks. J. Stat. Mech. *2008*, 10008. https://doi.org/10.1088/1742-5468/2008/10/P10008.

46. Hunter, J.D. (2007). Matplotlib: A 2D graphics environment. Comput. Sci. Eng. *9*, 90–95.

47. Thévenaz, P., Ruttimann, U.E., and Unser, M. (1998). A Pyramid Approach to Subpixel Registration Based on Intensity. IEEE Trans. Image Process. *7*, 27–41.

48. Bankhead, P., Loughrey, M.B., Fernández, J.A., Dombrowski, Y., McArt, D.G., Dunne, P.D., McQuaid, S., Gray, R.T., Murray, L.J., Coleman, H.G., et al. (2017). QuPath: Open source software for digital pathology image analysis. Sci. Rep. *7*, 16878. https://doi.org/10.1038/s41598-017-17204-5.

49. Wolf, F.A., Angerer, P., and Theis, F.J. (2018). SCANPY: large-scale single-cell gene expression data analysis. Genome Biol. *19*, 15. https://doi.org/10.1186/s13059-017-1382-0.

50. Lun, A.T.L., Bach, K., and Marioni, J.C. (2016). Pooling across cells to normalize single-cell RNA sequencing data with many zero counts. Genome Biol. *17*, 75. https://doi.org/10.1186/s13059-016-0947-7.

51. Wolock, S.L., Lopez, R., and Klein, A.M. (2019). Scrublet: Computational Identification of Cell Doublets in Single-Cell Transcriptomic Data. Cell Syst. *8*, 281–291.e9. https://doi.org/10.1016/j.cels.2018.11.005.

52. Waskom, M.L. (2021). seaborn: statistical data visualization. J. Open Source Software *6*, 3021. https://doi.org/10.21105/joss.03021.

53. Stuart, T., Butler, A., Hoffman, P., Hafemeister, C., Papalexi, E., Mauck, W.M., 3rd, Hao, Y., Stoeckius, M., Smibert, P., and Satija, R. (2019). Comprehensive Integration of Single-Cell Data. Cell *177*, 1888–1902.e21. https://doi.org/10.1016/j.cell.2019.05.031.

54. Palla, G., Spitzer, H., Klein, M., Fischer, D., Schaar, A.C., Kuemmerle, L.B., Rybakov, S., Ibarra, I.L., Holmberg, O., Virshup, I., et al. (2022). Squidpy: a scalable framework for spatial omics analysis. Nat. Methods *19*, 171–178. https://doi.org/10.1038/s41592-021-01358-2.

55. Dobin, A., Davis, C.A., Schlesinger, F., Drenkow, J., Zaleski, C., Jha, S., Batut, P., Chaisson, M., and Gingeras, T.R. (2013). STAR: ultrafast universal RNA-seq aligner. Bioinformatics *29*, 15–21. https://doi.org/10.1093/bioinformatics/bts635.

56. Schmidt, U., Weigert, M., Broaddus, C., and Myers, G. (2018). Cell Detection with Star-Convex Polygons. In Medical Image Computing and Computer Assisted Intervention – MICCAI 2018, A. Frangi, J. Schnabel, C. Davatzikos, C. Alberola-López, and G. Fichtinger, eds. (Springer International Publishing), pp. 265–273. https://doi.org/10.1007/978-3-030-00934-2_30.

57. Therneau, T.M., and Grambsch, P.M. (2000). Modeling Survival Data: Extending the Cox Model (Springer).

58. Blom, S., Paavolainen, L., Bychkov, D., Turkki, R., Mäki-Teeri, P., Hemmes, A., Välimäki, K., Lundin, J., Kallioniemi, O., and Pellinen, T. (2017). Systems pathology by multiplexed immunohistochemistry and

whole-slide digital image analysis. Sci. Rep. *7*, 15580. https://doi.org/10.1038/s41598-017-15798-4.

59. Jackson, H.W., Fischer, J.R., Zanotelli, V.R.T., Ali, H.R., Mechera, R., Soysal, S.D., Moch, H., Muenst, S., Varga, Z., Weber, W.P., and Bodenmiller, B. (2020). The single-cell pathology landscape of breast cancer. Nature *578*, 615–620. https://doi.org/10.1038/s41586-019-1876-x.

60. Tirosh, I., Izar, B., Prakadan, S.M., Wadsworth, M.H., 2nd, Treacy, D., Trombetta, J.J., Rotem, A., Rodman, C., Lian, C., Murphy, G., et al. (2016). Dissecting the multicellular ecosystem of metastatic melanoma by single-cell RNA-seq. Science *352*, 189–196. https://doi.org/10.1126/science.aad0501.

61. Jin, S., Guerrero-Juarez, C.F., Zhang, L., Chang, I., Myung, P., Plikus, M.V., and Nie, Q. (2021). Inference and analysis of cell-cell communication using CellChat. Nat. Commun. *12*, 1088.

62. Armingol, E., Officer, A., Harismendy, O., and Lewis, N.E. (2021). Deciphering cell-cell interactions and communication from gene expression. Nat. Rev. Genet. *22*, 71–88. https://doi.org/10.1038/s41576-020-00292-x.

Please cite this article in press as: Punovuori et al., Multiparameter imaging reveals clinically relevant cancer cell-stroma interaction dynamics in head and neck cancer, Cell (2024), https://doi.org/10.1016/j.cell.2024.09.046

CellPress
OPEN ACCESS

STAR★METHODS

KEY RESOURCES TABLE

REAGENT or RESOURCE	SOURCE	IDENTIFIER
Antibodies		
Rabbit Polyclonal Anti-AREG	LSBio	Cat#LS-B13911; RRID:AB_3106998
Mouse Monoclonal Anti-actin (Smooth Muscle)(αSMA) (Clone 1A4)	Dako	Cat#M0851; RRID: AB_2223500
Mouse Monoclonal Anti-Beta-Catenin (Clone 14)	Cell Marque	Cat#224M-14; RRID: AB_1158971
Rabbit Monoclonal Anti-Bmi-1 (Clone D20B7)	Cell Signaling Technologies	Cat#6964; RRID: AB_10828713
Rabbit Monoclonal Anti-CD11b (Clone EP45)	BioSB	Cat#BSB6441; RRID: AB_3107001
Rabbit Monoclonal Anti-CD3 (Clone EP449E)	Invitrogen	Cat#MA5-14482; RRID: AB_10985777
Mouse Monoclonal Anti-CD34 Class II (Clone QBEnd10)	Dako	Cat#M716529-2; RRID: AB_2063006
Mouse Monoclonal Anti-E-Cadherin (Clone 36)	BD Biosciences	Cat#610182; RRID: AB_397581
Rabbit Monoclonal Anti-EGFR (Clone D38B1)	Cell Signaling Technologies	Cat#:4267; RRID: AB_2864406
Rabbit Polyclonal Anti-Epcam	Abcam	Cat#71916; RRID:AB_1603782
Rabbit Monoclonal Anti-Fibroblast Activation Protein (FAP) (Clone EPR20021)	Abcam	Cat#:207178; RRID:AB_2864720
Guinea Pig Polyclonal Anti-Keratin 14	Progen	Cat#03-GP-CK14; RRID:AB_1541011
Mouse Monoclonal Anti-Keratin 18/8 (Clone C51)	Cell Signalling Technologies	Cat#4546; RRID:AB_2134843
Rabbit Polyclonal Anti-non-muscle Myosin Heavy Chain II-A (Myh9)	Biolegend	Cat#909802; RRID:AB_291638
Mouse Monoclonal Anti-pan-Cytokeratin (Clone C11)	Abcam	Cat#ab7753; RRID:AB_306047
Mouse Monoclonal Anti-Pan-Cytokeratin (Clone AE1/AE3)	Invitrogen	Cat#MA5-13156; RRID:AB_10983023
Rabbit Monoclonal Anti-PDGF Receptor Beta (Clone 28E1)	Cell Signalling Technologies	Cat#3169; RRID:AB_2162497
Rabbit Monoclonal Anti-Slug (Clone C19G7)	Cell Signalling Technologies	Cat#9585; RRID:AB_2239535
Rabbit Monoclonal Anti-Sox2 (Clone D6D9)	Cell Signalling Technologies	Cat#3579; RRID:AB_2195767
Rat Monoclonal Anti-Tenascin C (Clone 578)	R&D	Cat#MAB2138; RRID:AB_2203818
Mouse Monoclonal Anti-vimentin (Clone V9)	Santa Cruz Biotechnology	Cat#sc-6260; RRID:AB_628437
Biological Samples		
HNSCC Tumor Microarray 2005–2010	Auria Biobank pathology archive; Routila et al.[35]	AB15-7642
HNSCC Tumor Microarray 2005–2015	Auria Biobank pathology archive; Mylly et al.[36]	AB19-6863, ABTMA21-06

(*Continued on next page*)

Please cite this article in press as: Punovuori et al., Multiparameter imaging reveals clinically relevant cancer cell-stroma interaction dynamics in head and neck cancer, Cell (2024), https://doi.org/10.1016/j.cell.2024.09.046

Continued

REAGENT or RESOURCE	SOURCE	IDENTIFIER
Freshly Resected Human HNSCC Tissue	Helsinki University Hospital Head and Neck Center	N/A
Chemicals, Peptides, and Recombinant Proteins		
A83-01	Tocris Bioscience	Cat#2939
TGFß1	R&D	Cat#7754-BH
Gefitinib	Sigma	Cat# SML1657
Critical Commercial Assays		
Lenti-X Packaging Single Shots (VSV-G)	Takara Bio	Cat#631276
Visium Spatial Gene Expression Slide & Reagent Kit	10x Genomics	Cat#PN-1000184
Visium Spatial Gene Expression Reagent Kit	10x Genomics	Cat# PN-1000186
Visium Library Construction Kit	10x Genomics	Cat#PN-1000190
BD Rhapsody WTA Reagent Kit	BD	Cat#633802
Illumina NextSeq 500 High Output Kit v2.5	Illumina	Cat#20024908
Deposited Data		
Spatial RNA Sequencing of Eight Tongue Squamous Cell Carcinomas	This paper	GEO: GSE251902
Single-Cell RNA Sequencing of Human Tongue Squamous Cell Carcinomas in Spheroid Culture with and without Human Cancer Associated Fibroblasts	This paper	GEO: GSE252265
Experimental Models: Cell Lines		
UTSCC25 Human Tongue Squamous Cell Carcinoma	Auria Biobank; Routila et al.[37]	N/A
UTSCC47 Human Tongue Squamous Cell Carcinoma	Auria Biobank; Routila et al.[37]	N/A
UTSCC74a Human Tongue Squamous Cell Carcinoma	Auria Biobank; Routila et al.[37]	N/A
UTSCC76a Human Tongue Squamous Cell Carcinoma	Auria Biobank; Routila et al.[37]	N/A
HNSCC Patient-Derived Cancer-Associated Fibroblast Line	Kaukonen et al.[38]	N/A
Patient-Derived "Healthy" Non-cancer-Associated Fibroblast Line	Kaukonen et al.[38]	N/A
UTSCC74-eGFP Tagged Human Tongue Squamous Cell Carcinoma	This paper	N/A
UTSCC76-eGFP Tagged Human Tongue Squamous Cell Carcinoma	This paper	N/A
CAF-MCherry Tagged Human HNSCC-Derived Cancer-Associated Fibroblast	This paper	N/A
Experimental Models: Organisms/Strains		
Mouse: NOD.Cg-Prkdc^{scid} Il2rg^{tm1Wjl}/SzJ	Jackson Laboratory	Strain#005557; RRID:IMSR_JAX:005557
Recombinant DNA		
PLVX-EF1a-IRES-mCherry	Takara Bio	Cat# 631987
pLVX-EF1a-pIRES-EGFP	This paper	N/A
Software and Algorithms		
AnnData v0.9.1	Virshup et al.[39]	https://anndata.readthedocs.io/en/latest/index.html

(*Continued on next page*)

Continued

REAGENT or RESOURCE	SOURCE	IDENTIFIER
CellPhoneDB	Efremova et al.[40]	https://github.com/Teichlab/cellphonedb
CellProfiler v4.0.5	Stirling et al.[41]	www.cellprofiler.org
Commot v0.0.3	Cang et al.[25]	N/A
Fastp v0.23.2	Chen[42]	https://doi.org/10.1002/imt2.107
GraphPad v9.2.0	GraphPad Software	N/A
Harmony v0.0.9	Korsunsky et al.[43]	N/A
Ilastik v1.3.2	Berg et al.[44]	https://www.ilastik.org/
Leiden Clustering	Traag et al.[17]	https://github.com/vtraag/leidenalg
Louvain Community Detection Algorithm	Blondel et al.[45]	https://github.com/jlguillaume/louvain
Matpotlib v3.8.3	Hunter[46]	https://matplotlib.org/
pyCirclize	https://moshi4.github.io/pyCirclize	https://moshi4.github.io/pyCirclize
pyStackReg 0.2.5	Thevenaz et al.[47]	https://pypi.org/project/pystackreg/
QuPath v0.2.3	Bankhead et al.[48]	https://qupath.github.io/
RStudio v2024.04.2	Posit Software	N/A
Scanpy v1.9.3	Wolf et al.[49]	https://scanpy.readthedocs.io/en/stable/
Scran v1.22.1	Lun et al.[50]	https://bioconductor.org/packages/release/bioc/html/scran.html
Scrublet v0.2.3	Wolock et al.[51]	https://github.com/swolock/scrublet
Seaborn v0.13.2	Waskom[52]	https://github.com/mwaskom/seaborn
Seurat v4.0.2	Stuart et al.[53]	https://satijalab.org/seurat/
SlideViewer v2.5	3D Histech	https://www.3dhistech.com/research/digital-microscopes-viewers/slideviewer/
Squidpy v1.4.1	Palla et al.[54]	https://squidpy.readthedocs.io/en/stable/
STAR v2.7.10a	Dobin et al.[55]	https://github.com/alexdobin/STAR
StarDist 0.5.0	Schmidt et al.[56]	https://github.com/stardist/stardist
Shap 0.42.1	Lundberg et al.[23]	https://shap.readthedocs.io/en/latest/
Survival v3.1-12	Therneau and Grambsch[57]	https://CRAN.R-project.org/package=survival.
Other		
U-Bottom Ultra-Low Attachment 96-Well Plate	Corning	Cat#4520
CellTracker ™ Green CMFDA Dye	Invitrogen	Cat#C2925
CellTracker™ Orange CMRA Dye	Invitrogen	Cat#C34551
Rat Tail Collagen	Millipore	Cat#08-115
Matrigel Matrix	Corning	Cat#354230

EXPERIMENTAL MODEL AND STUDY PARTICIPANT DETAILS

Patient samples

The study and utilization of human tissue samples were approved by the Finnish national authority for medicolegal affairs (V/39706/2019), regional ethics committee of University of Turku (51/1803/2017) and Auria Biobank scientific board (AB19-6863). Formalin-fixed and paraffin-embedded (FFPE) tumor samples were obtained from the pathology archives of Auria Biobank.

For the prospectively collected fresh tumor samples a Research Ethics Board approval was obtained at the Helsinki University Hospital (HUS/745/2021) and a research permission was granted (HUS/85/2021). For patients involved in the retrospective datasets, patient consent was waived due to retrospective nature of the data in accordance with approval from Finnish National Supervisory Authority for Welfare and Health and regional ethics committee of University of Turku. The authors affirm that the study was conducted following the rules of the Declaration of Helsinki of 1975, revised in 2013.

The patient population and associated tumor microarrays (TMAs) have been described previously.[35,36] In short, two cohorts (cohort 1- 212 patients; cohort 2 – 454 patients) of TMA blocks containing formalin-fixed paraffin-embedded (FFPE) samples from patients treated for new HNSCC in the Turku University Hospital region between 2005-2015 with known TNM staging and survival end-points were used. Final TMA blocks of duplicate 1.2 mm cores were made in TMA Grand Master (3D Histech). For fresh-frozen

patient samples (spatial transcriptomics) eight patient biopsies from oral tongue SCC from primary surgery at the Helsinki University Hospital Head and Neck Center in 2022 were snap-frozen without fixation in OCT medium.

Cancer cell lines

Human tongue squamous cell carcinoma cells UTSCC74a (isolated from a 31y-old male with T3N1M0 G1-2 primary tumor), UTSCC76a (isolated from a 52y-old male with T3N0M0 G2 primary tumor), UTSCC25 (isolated from a 50y-old male with T2N0M0 G1 recurring tumor) and UTSCC47 (isolated from a 78y-old male with T2N0M0 G3 primary tumor) have been described earlier[37] and were obtained from Auria Biobank. CAFs were isolated from a T2N2bM0 G1 primary tumor of the buccal mucosa as previously described.[38] Paired healthy fibroblasts were isolated from the same patient as previously described.[38] Cells lines were maintained in DMEM (4500, mg/L glucose, 1x GlutaMAX, Gibco) supplemented with 1x non-essential amino acids (Gibco), 1x penicillin/streptomycin (Gibco) and 10% fetal bovine serum (Sigma-Aldrich).

eGFP-tagged UTSCC and mCherry-tagged CAF cell lines were generated through lentiviral transfection of the cells with a PLVX-EF1a-IRES-mCherry (Takara Bio) or pLVX-EF1a-pIRES-EGFP (cloned in-house by replacing mCherry from Takara Bio plasmid with EGFP) or plasmids, respectively, using the LentiX SingleShot transfection system (Takara Bio). After initial infection and expansion, eGFP and mCherry-expressing cells were purified using flow cytometry sorting.

METHOD DETAILS

Patient samples

TMA Cohort 1

The patient population and associated tumor microarrays (TMAs) have been described previously.[35] In short, ten TMA blocks containing formalin-fixed paraffin-embedded (FFPE) samples from patients treated for new HNSCC in the Turku University Hospital region between 2005-2010 with known TNM staging and survival end-points. A total of 212 patients were included in the study. While most tissue samples contained in the TMA came from primary (diagnostic) biopsies, a minority of samples also came from secondary tumors, including lymph node metastases, tumors resected following pre-operative radiotherapy, and recurrent tumors resected months or years following primary diagnosis and treatment. Multiple (1-8) cores were present on the TMA slide for some biopsies, and some patients were represented in the dataset by both primary and secondary samples. Each slide additionally contained a number of liver cores used by pathologists to orient the block; these samples were also analyzed within our study and were used to control for slide-to-slide variation in the dataset. Final TMA blocks of duplicate 1.2 mm cores were made in TMA Grand Master (3D Histech).

Numbers and types of biopsies used in the study:

Biopsy type	Number of samples
Primary (diagnostic)	176
Resected following pre-operative radiotherapy	32
Lymph node metastasis	22
Recurrent	55

TMA Cohort 2

The patient population and TMAs have been described previously.[36] In short, eleven TMA blocks containing formalin-fixed paraffin-embedded (FFPE) samples from patients treated for new HNSCC in the Turku University Hospital region between 2005-2015 with known TNM staging and survival end-points. Primary biopsies from a total of 454 patient biopsies were analyzed, and 438 were assigned both an epithelial and stromal phenotypic signature based on successful staining of a sufficient number of cells in both compartments.

Fresh-frozen patient samples (spatial transcriptomics)

HNSCC samples were collected from eight patients with oral tongue SCC undergoing primary surgery at the Helsinki University Hospital Head and Neck Center in 2022 and snap-frozen without fixation in OCT medium. Samples were subsequently processed for 10xVisium spatial transcriptomics as described below.

Multiplexed fluorescent immunohistochemical staining and imaging

Multiplexed fluorescent immunohistochemical staining and imaging was performed in three cycles as previously described[58] for two sets of 8-10 antibodies and the nuclear marker DAPI (Figure 1A), stained on two serial TMA sections. After the first-round staining and whole-slide imaging of the TMAs, the fluorescence signal was bleached, and the antibodies from the first-round staining were denatured, after which the second-round staining was performed. The process was repeated for the third round of staining. Imaging was performed using a Zeiss Axio Scan.Z1 slide scanner, with each round of staining recorded as an independent.CZI image file

Please cite this article in press as: Punovuori et al., Multiparameter imaging reveals clinically relevant cancer cell-stroma interaction dynamics in head and neck cancer, Cell (2024), https://doi.org/10.1016/j.cell.2024.09.046

containing up to five fluorescent channels. Markers were selected based on published expression of genes in HNSCC[8] and most commonly used markers for CAFs.[27] EMT markers were based on high reported expression of vimentin and SNAIL2 and lack of substantial expression of "classical" EMT markers such as EMT TFs, ZEB1/2, TWIST1/2, and SNAIL1.[8]

Antibodies used in the study:

Antibody target	Supplier and catalogue number	Dilution, staining time and temperature
AREG	LSBio LS-B13911	1:100, 1h Room temperature (RT)
αSMA	Dako M0851	1:500, 2h RT
ß-catenin	Cell Marque 224M-14	1:500, 1.5h RT
Bmi-1	Cell Signalling Technologies 6964	1:100, 1.5h RT
CD11b	Bio SB 6441	1:200, Overnight 4°C
CD3	Invitrogen MA5-14482	1:750, Overnight 4°C
CD34	Dako M716529-2	1:200, Overnight 4°C
E-cadherin	BD 610182	1:200, 2h RT
EGFR	Cell Signalling Technologies 4267	1:200, 2h RT
Epcam	Abcam 71916	1:500, 2h RT
FAP	Abcam 207178	1:1000, 2h RT
Keratin 14	Progen GP-CK14	1:200, 2h RT
Keratin 18/8	Cell Signalling Technologies 4546	1:50, 2h RT
Myh9	Biolegend Poly 909801	1:2000, 1h RT
Pan-cytokeratin	Abcam 7753	1:150, 2h RT
Pan-cytokeratin	Invitrogen MA5-13156	1:100, 2h RT
PDGFRB	Cell Signalling Technologies 3169	1:100, 1.5h RT
Slug	Cell Signalling Technologies 9585	1:50, 1.5h RT
Sox2	Cell Signalling Technologies 3579	1:100, 2h RT
Tenascin C	R&D MAB 2138	1:100, 1.5h RT
Vimentin	Santa Cruz Biotechnology SC6260	1:200, 2h RT

Automated image analysis pipeline for processing large multiplexed TMA datasets

Images of individual TMA cores were extracted from the whole-slide images using the TMA dearrayer functionality in QuPath.[48] Images from the three staining rounds were registered using an affine image registration method operating through the pyStackReg[47] Python dependency, aligning the DAPI channels of the three staining rounds. Autofluorescence signal from red blood cells and other histology artefacts (e.g. wrinkled or folded tissue section areas) were removed using a pixel classifier in Ilastik.[44] Nuclei were segmented from the DAPI channel using a trained StarDist model.[56] The nuclear regions of interest (ROIs) were expanded by 6 pixels to generate cytoplasmic ROIs. A python script was then used to calculate fluorescence intensity in all channels, nuclear morphometric features, and local neighborhood parameters.

Parameter set used to assign phenotypic clusters:

Parameter	Epithelial panel	Stromal panel
Nuclear mean intensity	DAPI, Slug, Bmi1, Sox2	DAPI
Cytoplasmic mean intensity	ß-catenin, KRT8/18, KRT14, Epcam, Vimentin	PDGFRB-ß, CD11b, CD34, CD3, α-SMA, FAP, Pan-cytokeratin, EGFR
Morphometric parameters	Area, circularity, roundness, perimeter, solidity, compactness, aspect ratio, EFC ratio	
Local neighborhood parameters	Order, number of neighbors (nuclei within 85 pixels to each other in centroid-to-centroid distance), distance to nearest neighbor, distance to nearest epithelial/stromal cell	

Single-cell clustering of cell phenotypes

The above-described cellular and local neighborhood features were treated as individual parameters that together define cellular phenotypes. A Pearson's correlation analysis was used to compare the correlation of each parameter to all other parameters, and highly correlated (and therefore redundant) parameters were removed from the analysis. The remaining parameters were formatted as a "count

Please cite this article in press as: Punovuori et al., Multiparameter imaging reveals clinically relevant cancer cell-stroma interaction dynamics in head and neck cancer, Cell (2024), https://doi.org/10.1016/j.cell.2024.09.046

matrix" and analyzed using the Seurat package in R.[53] All parameter values were normalized to remove sampling effect and scaled to obtain relative parameter expression between cells. To identify cells with similar phenotypes, principal component analysis (PCA) was performed, followed by UMAP dimensionality reduction to visualize the similarities and differences between all cells in the dataset.

By analyzing the expression of key epithelial and stromal markers, we found that single-cell clustering was a robust method for differentiating epithelial tumor cells from stromal cells of the microenvironment. Based on their cluster assignment, each cell was given a label denoting its epithelial (tumor) or stromal identity. Using these labels, the distance (in pixels) of each epithelial cell to the nearest stromal cell (and vice versa) was calculated using a custom python script, and this parameter was added to the global parameter set.

With this complete parameter set, the single-cell clustering was repeated separately on the stromal and epithelial compartments. Cluster stability was evaluated by examining dispersion of differentially expressed markers; where bimodal distributions were observed in the largest clusters, clustering resolution was increased until unimodal distributions were observed. The major clusters that captured >90% of the cells in all patients in the respective compartments were annotated and used in subsequent analyses.

Next, the relative proportions of each cluster in any given biopsy were quantified, constituting the tumor "signature". For biopsies represented by multiple TMA cores, all cells were pooled together to gain the most representative view of the whole tumor. Samples containing fewer than 100 epithelial or stromal cells were excluded from the respective analysis. Patients were then stratified into subgroups based on the similarities of their phenotypic signatures using a Pearson's correlation approach. In order to assign the phenotypic signatures in an unbiased way, several clustering resolutions were used, and the patient groups that most robustly clustered together formed the final major signatures.

Tumor architecture analyses

Border-center analysis

For quantifying marker expression at tumor borders compared to the tumor core, epithelial cells that were within 120 pixels (26 μm) of a stromal cell in centroid-to-centroid distance were designated as "border" cells; all other epithelial cells were designated as central cells. Mean expression of selected markers was then quantified within these two compartments per patient.

Inter-cluster distances analysis

First, epithelial and stromal cell centroids from adjacent tissue sections were co-registered by utilizing the DAPI signals from adjacent tissue sections as input of a rigid registration algorithm to compute the transformation matrix. The transformation matrix was applied to the stromal cell centroids and the registration quality was visually assessed for each section. Then, for each combination of tumor-stroma clusters, shortest pairwise Euclidean distances between tumor and stroma centroids were computed. Kernel density estimates were then generated for visualizing and comparing distributions of multiple pair of tumor-stroma clusters simultaneously.

Architecture analyses

For measuring tumor architectures, tumor compartments were partitioned into spatial subunits based on their topological neighborhood graphs.[59] First, neighbors of each tumor cell within a given radius of R=16μm (2-3 cell diameters) were queried using the Ball-Tree algorithm and the topological neighborhood graph of each tumor section was generated. This graph was then input to the Louvain community detection algorithm[45] to detect tissue subunits. Finally, the fragmentation index was computed as the average number of tumor cells per subunit divided by the total number of tumor cells in the section.

CAF subclustering

CAF cells were isolated from the stromal clustering and re-clustered based on their expression of FAP, aSMA, COL1 and PDGRFA using the Leiden algorithm.

Survival analysis

Kaplan-Meier analysis was performed using Survival v3.1-12[57] to compare survival outcomes between patient groups with different phenotypic signatures, with Log-rank test used to measure statistical significance. A Cox proportional hazard model was used to quantify the impact of different clinical variables, including a patient's phenotypic signature, on survival probability. For both tests, $p \leq 0.05$ was used as a cut-off for statistical significance.

Spatial transcriptomics

HNSCC samples were collected from patients undergoing surgery at the Helsinki University Hospital in 2022. Clinical details are summarized below:

Patient No	Sex	Ethnicity	Age at diagnosis	TNM staging
UH8	Male	Caucasian	22	T2N0M0
UH12	Female	Caucasian	54	T2N1M0
UH17	Male	Caucasian	37	T3N2M0, G3
UH19	Female	Caucasian	86	T3N2aM0
UH20	Female	Caucasian	68	T4N0M0

(*Continued on next page*)

Continued

Patient No	Sex	Ethnicity	Age at diagnosis	TNM staging
UH21	Male	Caucasian	66	T2N0M0, G2
UH22	Female	Caucasian	69	T2N0M0
UH24	Male	Caucasian	64	T3N2bM0, G2

The samples were snap-frozen in OCT medium without fixation, sectioned, fixed in 4% PFA and stained for the expression of Keratin 14, Vimentin and CD3. Eight tongue carcinoma patient samples representing the distinct phenotypes (pEMT neg/pos, CAF vs immune-enriched stroma; 2 each) were subjected to spatial transcriptomics analysis.

For this, 10 μm cryosections were mounted onto the ST arrays (10X Genomics Visium) and stored at −80°C until use. Tissue sections were fixed in methanol at –20°C and then stained with hematoxylin and eosin. Permeabilization was optimized according to the manufacturers' instructions and a 10 min time was selected after which polyadenylated RNAs captured on the arrays were resuspended in 1.2 ml of 0.1 N HCl for 5 min and reverse transcribed at 53°C for 45 min, followed by second-strand synthesis at 65°C for 5 min. After library preparation, samples were sequenced on a Novaseq 600 (Illumina).

Sequencing output and the histology images were processed using Space Ranger software (10X Genomics). The space ranger mkfastq function was used for sample demultiplexing and for converting spatial barcodes and reads into Fastq format. The space ranger count function was used to align reads to the human genome (hg38) and with the microscopic slide image, to generate quality-filtered barcode/UMI counts, and feature spot matrices for gene expression analysis.

Raw counts were imported as AnnData[39] objects using Squidpy (1.4.1[54]), "read_visium". Each sample's gene expression matrix was normalized using scran (1.22.1[50]) with Leiden clustering[17] input at resolution 0.5. Spots were manually filtered for isolated or detached tissue regions due to missing spatial context.

G2M and S phase scores were assigned to each cell using published gene lists[60] and the Scanpy (1.9.8[49]) "scanpy.tl.score_genes_cell_cycle" function.

At this stage samples were merged. For 2D embedding and clustering, we first regressed G2M and S-phase scores out of the normalized gene expression matrix using "scanpy.pp.regress_out". The matrix was then subset to the 3,000 most highly variable genes (scanpy.pp.highly_variable_genes, flavor "seurat"). The top 100 principal components (PCs) were calculated, and batch-corrected using Harmony (0.0.9[43]). The PCs served as basis for k-nearest neighbor calculation (scanpy.pp.neighbors, n_neighbors=30), which were used as input for UMAP[18] layout (scanpy.tl.umap, min_dist=0.3).

Cells were clustered using the Leiden algorithm at resolution 0.6 using scanpy.tl.leiden, and annotated manually on the basis of known marker genes.

Ligand-receptor interactions were calculated using CellphoneDB[40] using the "squidpy.ge.ligrec" implementation. Pathway annotations were obtained from Jin et al.[61] from the GitHub repository https://github.com/LewisLabUCSD/Ligand-Receptor-Pairs.[62]

Overall numbers of ligand-receptor interactions between cell populations were visualized using pyCirclize (https://moshi4.github.io/pyCirclize), where link width and color are proportional to the number of significant interactions with a P-value cutoff of 0.1. Pathway-specific enrichment of interactions was plotted using Matplotlib (3.8.3[46]) "imshow". Significant interactions (P<0.1) were split into "sending" and "receiving" for each cell population, counted per pathway, and finally z-transformed.

COMMOT (0.0.3[25]) was used to calculate spatial interactions scores for select pathways using "commot.tl.spatial_communication" with "dis_thr=500". Results were visualized using "squidy.pl.spatial_scatter" and seaborn (0.13.2[52]), violin plots, showing receiver and sender score sums.

Cancer cell / CAF 3D co-spheroids

For 3D co-culture spheroid studies, eGFP and mCherry-tagged cells were plated as single-cell suspensions into U-bottom ultra-low attachment 96-well plates (Corning 4520) in the medium described above. Each well contained approximately 1000 cells; for co-culture studies, approximately 750 CAFs and 250 UTSCC cells were plated per well. After plating, the plate was centrifuged at 300 x g for one minute to collect all cells at the bottom in close proximity to one another. Co-cultures were cultured at 37°C, 5% CO_2 for up to 48h.

For inhibitor experiments, cells were pre-treated for 72h with 10μM of A83-01 (Tocris), 10ng/mL of recombinant human TGFß1 (R&D) or with 1:1000 DMSO as a control. For EGFR inhibition experiments, cells were additionally pre-treated with 500nM Gefitinib (Sigma) for 72h.

Imaging and image analysis

3D co-culture spheroids were live-imaged on an Opera Phenix high-content screening system (PerkinElmer) using 20x air, 40x air and 40x water-immersion objectives. Spheroids were imaged as 3D confocal stacks of 25 planes at 4μm intervals. For live-imaging studies, spheroids were images hourly for up to 16h.

For quantification of eGFP intensity at spheroid cores, a representative confocal plane through the spheroid center was selected. The spheroid core was manually outlined and mean eGFP intensity was measured in ImageJ. This was normalized to eGFP signal at

the rim of the spheroid, quantified by manually outlining the rim at a thickness of 30 pixels for images acquired on a 20x objective and 60 pixels for images acquired on a 40x objective.

Cells cultured in 2D monolayers were fixed for 15 min at room temperature in 4% paraformaldehyde (PFA) pre-warmed to 37°C, blocked for 1h 3% bovine serum albumin, 5% normal goat serum, 0.03% Triton-X in PBS at room temperature, and stained using primary and secondary antibodies for 1h at room temperature. Plates were then imaged on an Opera Phenix high-content screening system (PerkinElmer) using a 10x air objective. Mean nuclear and cytoplasmic expression of proteins was quantified using CellProfiler software.[41]

Single-cell RNA sequencing and analysis

HNSCCs and CAFs were co-cultured for 48h as described above, after which single cell suspensions were generated by incubation of spheroids with 0.5% Trypsin/0.5mM EDTA (Gibco) for up to one hour at 37°C. After washing with ice-cold DMEM, single cells were counted using Luna-II automated cell counter (Logos Biosystems) and loaded on a microwell cartridge of the BD Rhapsody Express system (BD) following the manufacturer's instructions. Single cell whole transcriptome analysis libraries were prepared according to the manufacturer's instructions using BD Rhapsody WTA Reagent kit (BD, 633802) and sequenced on the Illumina NextSeq 500 using High Output Kit v2.5 (150 cycles, Illumina) for 2 × 75 bp paired-end reads with 8 bp single index aiming sequencing depth of >20,000 reads per cell for each sample.

Analysis

Raw FASTQ reads were quality trimmed using fastp[42] (version 0.23.2; length cutoff 20, quality cutoff 15). The UMI, complex barcode, and sample tags were extracted and demultiplexed using custom scripts. Reads were mapped using STAR version 2.7.10a.[55]

Raw counts were imported as AnnData[39] (v. 0.9.1) objects in Python (3.10.3). We removed low complexity barcodes with the knee plot method (7000-8000 counts per cell), and further filtered out cells with a high mitochondrial mRNA percentage. Doublets were predicted with scrublet[51] (v. 0.2.3). Finally, each sample's gene expression matrix was normalized using scran[50] (v. 1.22.1), with Leiden clustering[17] input at resolution 0.5.

At this stage samples were merged with scanpy[49] (v. 1.9.3). For 2D embedding, the expression matrix was subset to the 3,000 most highly variable genes (sc.pp.highly_variable_genes, flavor "seurat"). The top 100 principal components (PCs) were calculated. The PCs served as basis for k-nearest neighbor calculation (sc.pp.neighbors, n_neighbors=30), which were used as input for UMAP layout (sc.tl.umap, min_dist=0.3).

3D invasion

Spheroids of 2500 cells were grown either as mono-cultures or as co-cultures with either CAFs or "healthy" non-cancer associated fibroblasts[38] in a ratio of 1:4 cancer cells to fibroblasts. UTSCC74 and 76 were stably expressing eGFP and CAFs mCherry. Green and orange CellTracker dyes (CellTracker™ Green CMFDA Dye C2925) were used to label UTSCC25 and UTSCC47 cells.

3mg/mL rat tail collagen I (Millipore 08-115) 3D hydrogels were prepared by mixing a 1:4 ratio of reconstitution buffer (0,26M NaHCO3, 0,2M HEPES, 1XHBSS, 0,05M NaOH) and collagen and adjusting the pH to 7.5. Spheroids were pre-cultured for 48h in suspension and then embedded in collagen to form 3D gels that were incubated for 48h before fixing with 4% paraformaldehyde (PFA) and imaging on Nikon Eclipse Ti2 microscope.

For inhibitor experiments, cancer cell lines were pretreated with 10μM A83-01for 48h prior to being seeded into spheroids containing 500 nM Gefitinib where indicated. Invasion was quantified by measuring mean cancer cell and CAF distance from the center of spheroid in four quadrants.

In vivo orthotopic transplantation

In vivo transplantation experiments were ethically assessed and authorised by the National Animal Experiment Board and in accordance with The Finnish Act on Animal Experimentation (Animal license number ESAVI/6253/2024). All efforts were made to minimize animal suffering and to reduce the number of animals used.

For injections, cells were isolated from spheroids cultured as described above and pooled from 4 plates (UTSSC) or sixteen plates (UTSSC+CAF). Spheroids were pelleted at 300 x g, washed once with 1.5 ml of PBS, followed by trypsinization for 30-40 min at +37ºC while suspending every 10 min to aid dissociation. After washing with media, a single cell suspension was prepared in PBS and the volume adjusted to ~200-300μl, depending on cell number. Prior to injection, 30% v/v growth-factor reduced Matrigel was mixed into the cell suspension and 30 μl of the mixture, containing 17 000 cancer cells alone or with 51000 CAFs (68 000 cells in total), was injected using an insulin syringe (0,3 ml, 0,30 mm (30G) x 8 mm; BD Micro-Fine) per mouse.

Immunocompromised mice (NOD.Cg-PrkdcscidIl2rgtm1Wjl/SzJ; Charles River) between 9-12 weeks of age were treated with painkiller and anti-inflammatory mixture (0,07 mg/kg Buprenorphine and 20 mg/kg Carprofen 100μl of PBS injected intraperitoneally) 30 min prior to tongue injection and twice a day for 3 days after injection. Mice were anesthetized (75 mg/kg Ketamine and 6 mg/kg Xylazine in 200μl of PBS injected subcutaneously) for injection of patient-derived cancer cells tagged with eGFP (UTSCC74 or UTSCC76) alone or with mCherry-tagged CAFs to the side of the tongue.

After injection, mice were given softened food ad libitum to ensure that they could eat regardless of tumor growth. Animal weight and tumor growth was closely monitored for two weeks (end point). Mice were sacrificed, and tongues with tumors were collected for fixation overnight with 10% formalin in phosphate buffer (FF-Chemicals). Tissues were embedded in paraffin and 4-5 μm sections were cut for hematoxylin-eosin and immunostainings.

Hematoxylin-eosin stainings were performed using standard protocols. For immunostainings paraffin sections were deparaffinized with two rounds of xylene, one round of 2-propanol, and graded ethanol series from 96% to 50%, each for 5 minutes, before washing the samples with cold tap water. Antigen retrieval was performed with indicated pH using Dako Target Retrieval Solution (Agilent) and 2100 Antigen retriever (Aptum Bio) following manufacturer instructions. Tissues were then permeabilized with 0.6% Triton in PBS solution for 10 min at room temperature and blocked with 0.3% Triton, 5% BSA in PBS solution for 1 h at room temperature. Sections were incubated with primary antibodies in a humidified chamber overnight at +4 °C, followed by a 1 h of appropriate secondary antibody incubation at room temperature. For subsequent stains following stain 1, coverslips were removed by rinsing slides in tap water, after which the slides were incubated in 1mM EDTA, pH 9.0 for 20 minutes at 95C. Following this, slides were cooled to room temperature with tap water and then blocked and subjected again to primary and secondary antibodies as above before the next round of imaging. Following each round of immunofluorescence staining, hydrophobic barrier was removed and the slides were coverslipped using ProLong Gold mounting medium (Invitrogen). Imaging was performed on Phenoimager (Akoya Biosciences) using a filter-set optimized for DAPI, AF488, AF594 and AF647 with a 20X objective with NA 0.75. Exposure times varied between 2-5 msec for DAPI and 80-200 msec for the rest of the fluorophores.

The following antibodies were used: AREG (LSBio LS-B13911, 1:100), Keratin-14 (Progen GP-CK14; 1:200), Slug (Cell Signaling 9585; 1:200), Sox (Cell Signaling 3579; 1:100), Vimentin (Santa Cruz SC6260; 1:200).

QUANTIFICATION AND STATISTICAL ANALYSIS

Statistical analyses were performed using GraphPad Prism software (version 9) or in R (version 2023.09.1+494). Statistical significance was determined by the specific tests indicated in the corresponding figure legends. Only 2-tailed tests were used. In all cases where a test for normally distributed data was used, normal distribution was confirmed with the Kolmogorov–Smirnov test ($\alpha = 0.05$). All experiments presented in the manuscript were repeated at least in 3 independent replicates.

CellPress
OPEN ACCESS

Supplemental figures

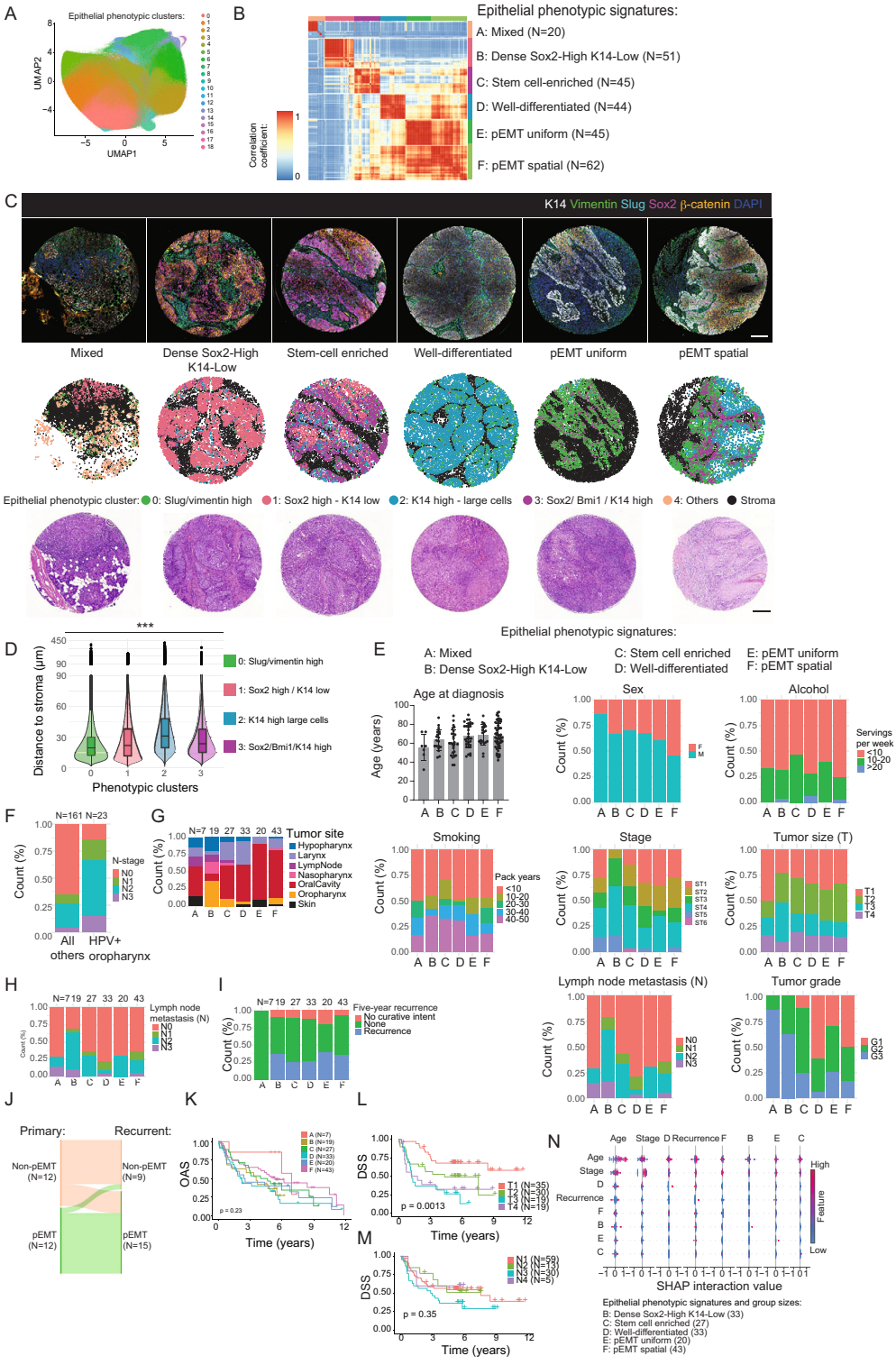

(legend on next page)

Figure S1. Analyses of tumor phenotypes and their clinical correlation, related to Figure 1

(A) UMAP plot of all stained cells from the epithelial panel.

(B) Pearson's correlation plot showing derivation of epithelial phenotypic signature groups. Each row and column represent one patient sample.

(C) Representative composite immunofluorescence images of the six merged channels, corresponding spatial projections, and H&E images of representative TMA cores of the six epithelial phenotypic clusters. Note that H&E and multiplex staining are not from adjacent sections. Scale bar, 200 μm.

(D) Quantification of distance to stroma from single cells across indicated epithelial phenotypic clusters. Note that cells with pEMT and stem-cell-like features are on average closer to the stroma than other phenotypes (n = 1,135,767 cells, $p < 0.001$; Kruskal-Wallis/Wilcoxon rank sum test with Bonferroni adjustment).

(E) Distribution of relevant clinical parameters across the six epithelial signatures.

(F) Distribution of lymph node metastasis (N-staging) in patients with HPV+ oropharyngeal tumors and all other primary tumors. HPV+ oropharynx patients have higher lymph node involvement at time of diagnosis.

(G) Distribution of primary tumor sites across the six epithelial phenotypic signatures. HPV+ oropharynx tumors removed.

(H) Distribution of lymph node metastasis (N-staging) at time of diagnosis across the six epithelial signatures in primary tumors. HPV+ oropharynx tumors removed.

(I) Distribution of tumor recurrence 5 years after diagnosis across the six epithelial phenotypic signatures in primary tumors. HPV+ oropharynx tumors removed. All patients who were treated without curative intent died within 3 years of diagnosis.

(J) Analysis of relationship between primary and recurrent epithelial pEMT status from patients with paired biopsies of primary and recurrent tumors. Note crossover of non-pEMT to pEMT state between a subset of primary and recurrent cases.

(K) Overall survival of patients based on the epithelial signature of their primary tumor; log-rank test. HPV+ oropharynx patients removed.

(L) Disease-specific survival of patients based on T-staging of their primary tumor; log-rank test. HPV+ oropharynx patients removed.

(M) Disease-specific survival of patients based on lymph node metastasis status (N-stage) at time of diagnosis; log-rank test.

(N) SHAP interaction values for the main epithelial signatures and predictive clinical variables. Each dot corresponds to an individual patient, and the dot position on the x axis shows the impact that this feature has on the model's prediction for that patient. No significant interaction with pEMT signatures and clinical parameters is observed.

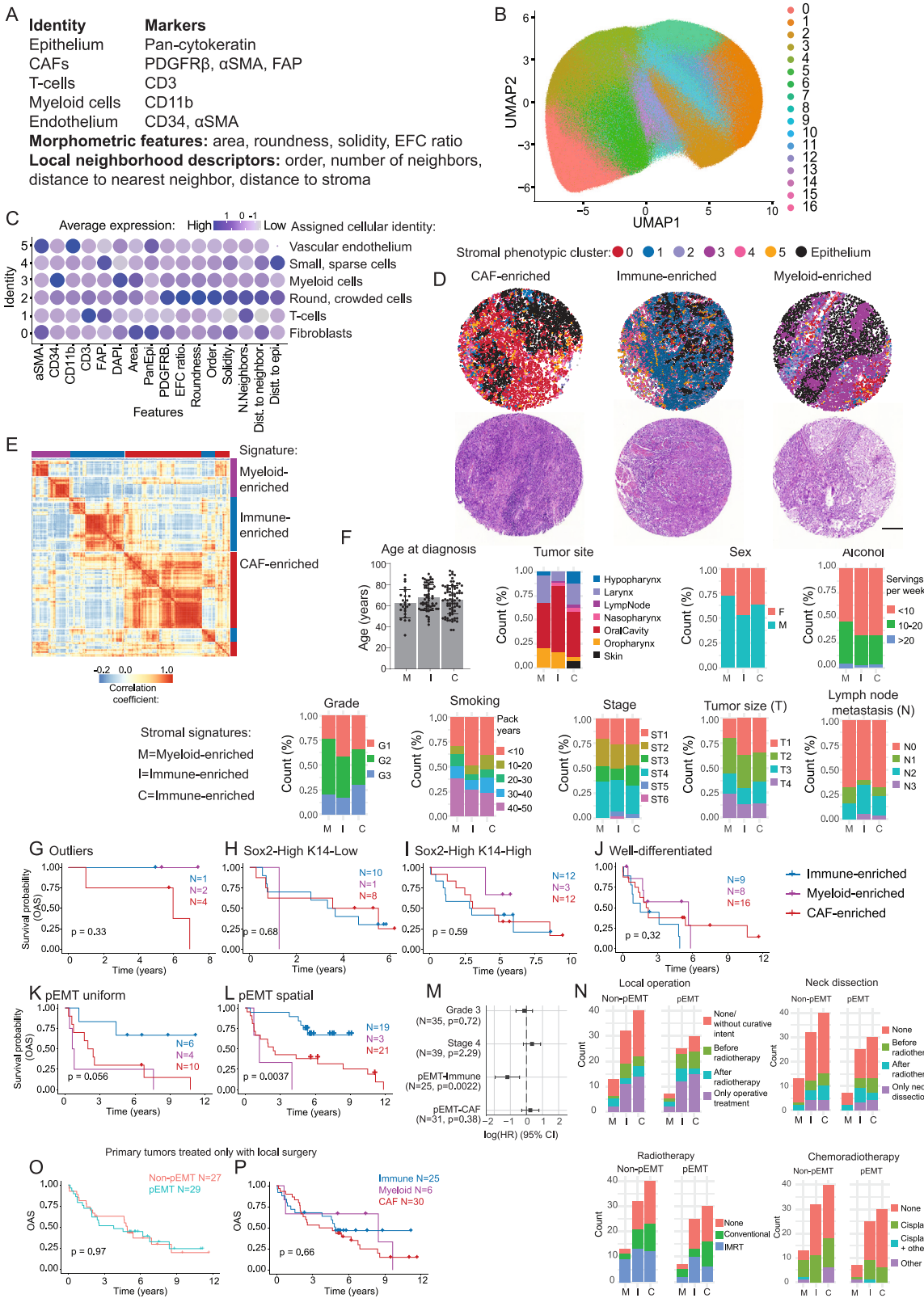

(legend on next page)

Figure S2. Analyses of stromal phenotypes and their clinical correlation, related to Figure 2

(A) Markers and parameters used in the stromal multiplexed immunofluorescence panel.

(B) UMAP plot of all cells stained with the stromal panel.

(C) Dot plot showing relative expression of each quantified feature within each stromal phenotypic cluster.

(D) Representative spatial projections of stromal phenotypic clusters and corresponding H&E images across the phenotypic signatures. Note that H&E and multiplex stainings are not from adjacent sections. Scale bar, 200 μm.

(E) Pearson's correlation plot showing the assignment of stromal phenotypic signatures. Rows and columns denote individual patient samples.

(F) Relevant clinical and histopathological features of primary tumors grouped by their stromal signature (on x axis); M, myeloid-enriched, I, immune-enriched, C, CAF-enriched.

(G–L) Disease-specific survival in all epithelial signature groups split by stromal signature; log-rank test. Sample grouping based on patients' primary biopsy. HPV+ oropharynx patients removed.

(M) Cox proportional hazard modeling of disease-specific survival for grade, stage, and the combined stromal-epithelial signature. HPV+ oropharynx patients removed.

(N) Distribution of treatments received by patients, split by the epithelial and stromal signatures of their primary biopsy. HPV+ oropharynx patients removed. M, myeloid-enriched, I, immune-enriched, C, CAF-enriched.

(O) Overall survival of patients receiving only local surgery grouped based the pEMT status of their primary tumor; log-rank test. HPV+ oropharynx samples removed.

(P) Overall survival of patients receiving only local surgery grouped based the stromal phenotypic signature of their primary tumor; log-rank test. HPV+ oropharynx samples removed.

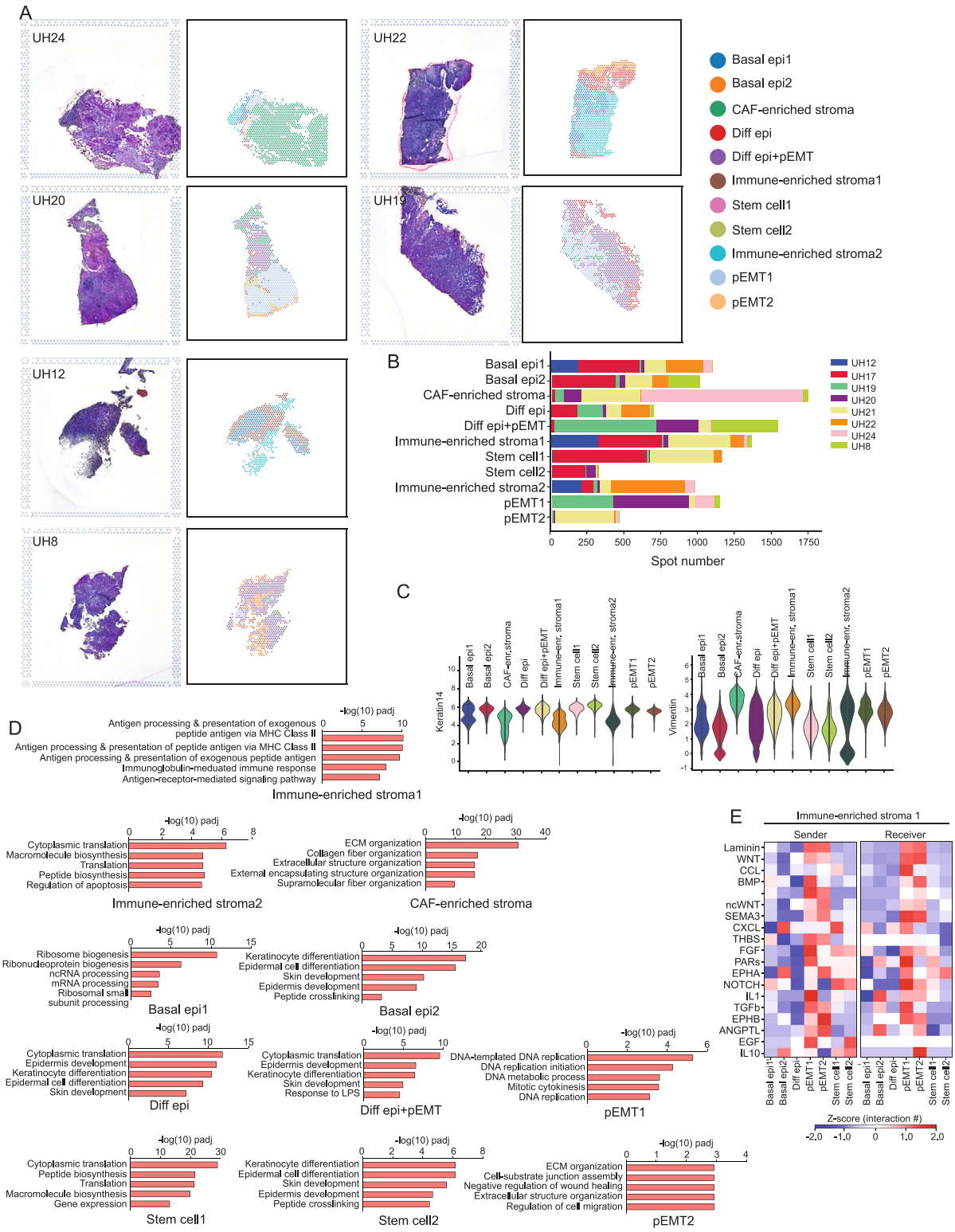

Figure S3. Spatial transcriptomic analyses from representative HNSCC biopsies, related to Figure 3

(A) H&E images and spatial projections of annotated Louvain clusters from spatial transcriptomics for the individual patient biopsies.

(B) Quantification of the distribution of the annotated Louvain clusters across the individual patient spots.

(C) Gene expression analysis for keratin 14 and vimentin across the clusters to determine stromal and epithelial identity.

(legend continued on next page)

(D) GO-term analyses of biological processes enriched in the marker gene sets of the annotated Louvain clusters.
(E) Heatmap of top differentially abundant (*Z* score) predicted receptor-ligand interactions sent and received from the immune-enriched stroma cluster 1 to all the epithelial clusters. Analysis is restricted to patients UH17, 20, and 21, where these clusters are present in abundance.

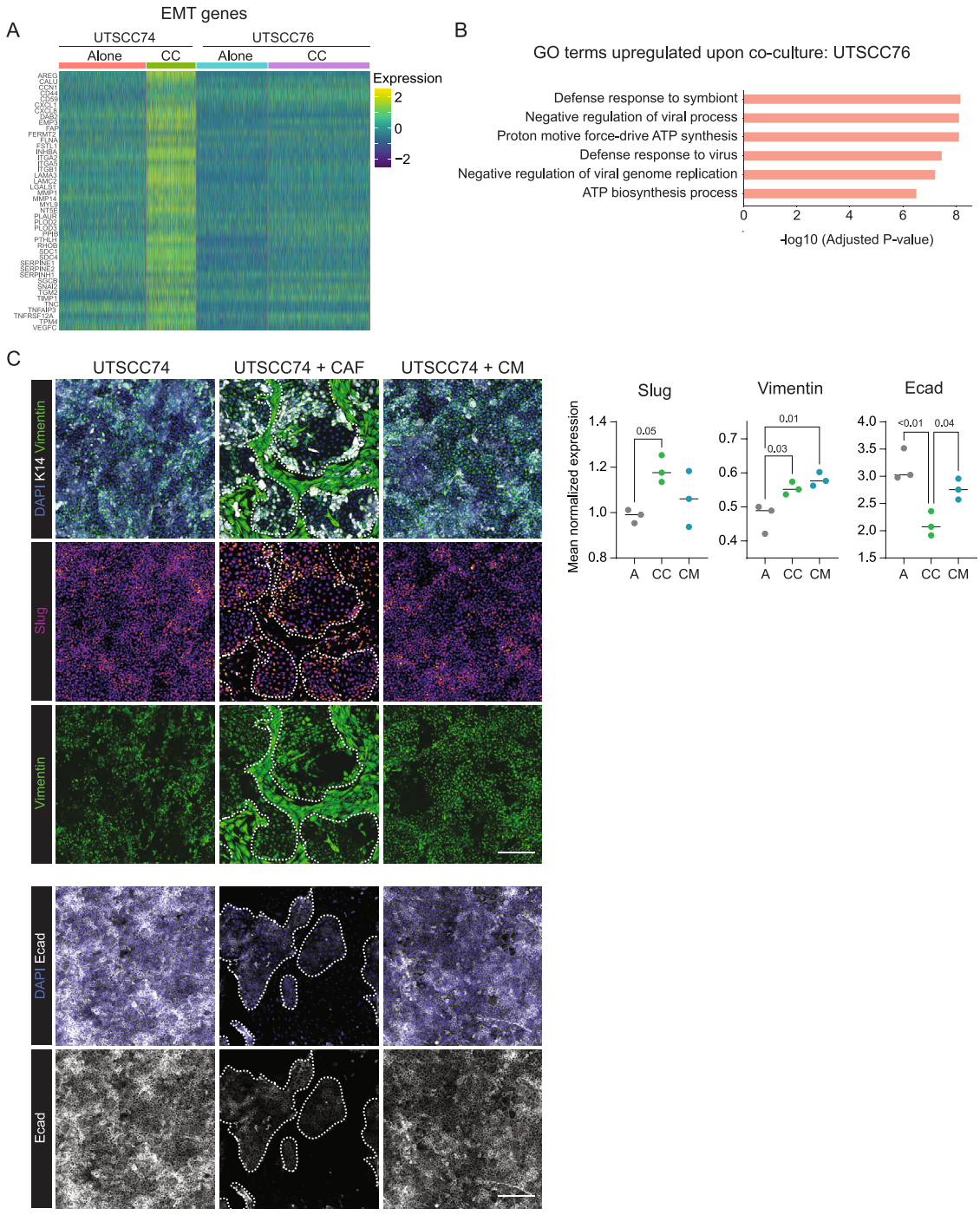

Figure S4. Analyses of HNSCC cell-CAF co-cultures, related to Figure 4

(A) Heatmap of changes in selected EMT gene expression in two different cancer cell lines cultured either alone or in co-culture (CC) with CAFs from single-cell RNA sequencing.

(B) GO terms enriched in differentially expressed genes of UTSCC76a cells co-cultured with CAFs compared with the same SCC cells cultured alone.

(C) Representative immunofluorescence images and quantification of UTSCC74 cells cultured alone (A) or together with CAFs (CC) or with CAF-derived conditioned medium (CM); dotted line denotes cancer/CAF border. Note that direct co-culture is required to enhance expression of Slug and suppress E-cadherin (scale bar, 100 μm; *n* = 3 independent experiments; one-way ANOVA/Tukey's).

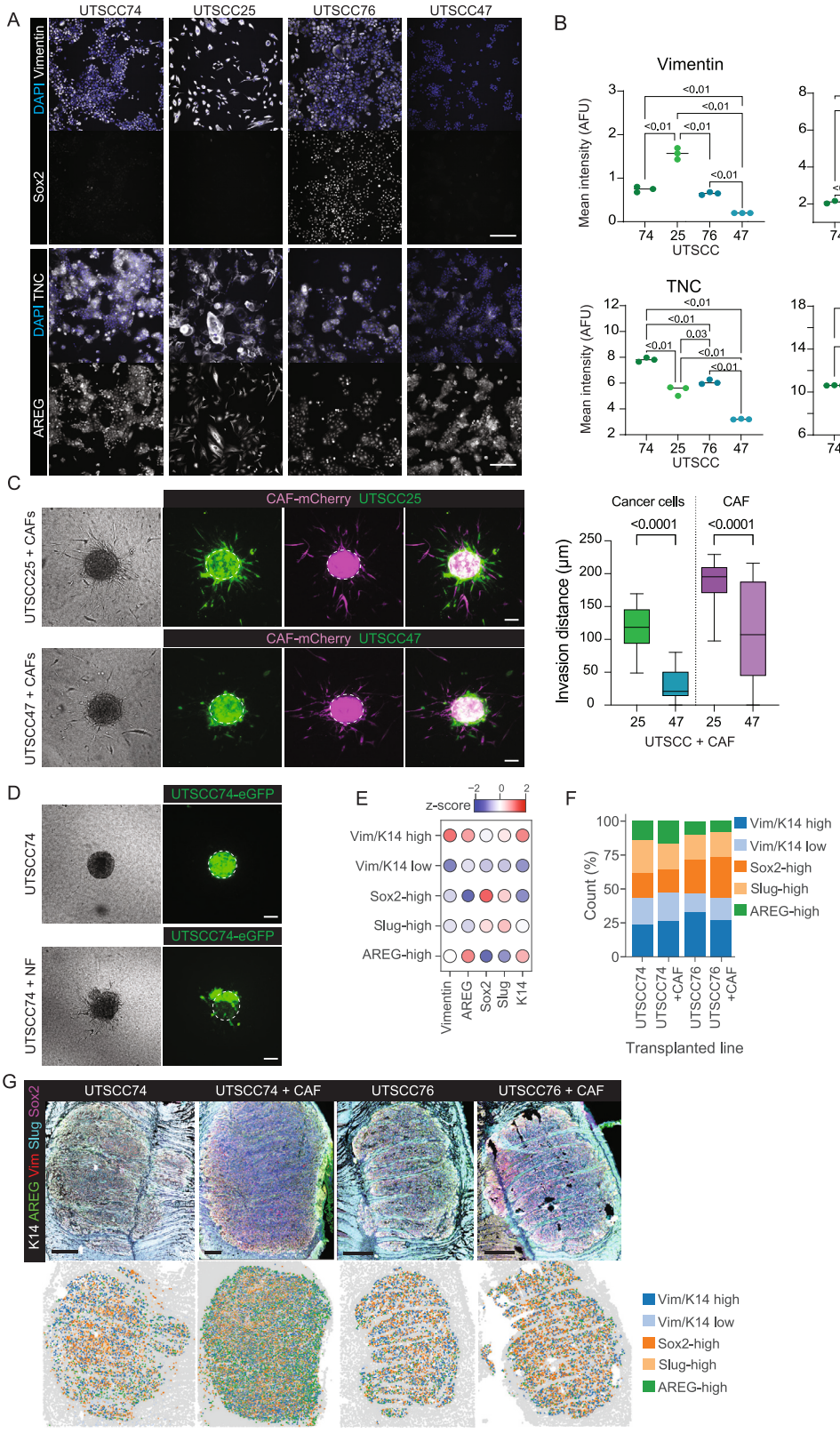

(legend on next page)

Figure S5. Analyses of tumor phenotypes and invasiveness in co-cultures and upon orthotopic transplantation, related to Figure 5

(A and B) Representative images (A) and quantification (B) of cytoplasmic vimentin, AREG, and TNC and nuclear Sox2 expression in four UTSCC cell lines. AFU, arbitrary fluorescence units. Note high expression of EMT markers in UTSCC74 and -25 and high Sox2 expression in UTSCC76 (n = 3 independent experiments; one-way ANOVA/Tukey's). Scale bar, 100 μm.

(C) Representative images of 3D invasion assays of CAF co-spheroids with pEMT-like UTSCC25 and non-pEMT-like UTSCC47 cells. Dashed white line outlines spheroid edge. Quantification shows average distance from spheroid edge measured in four quadrants. pEMT-like UTSCC25 co-cultured with CAFs show increased cancer cell invasion as compared with non-pEMT cell line UTSCC47 (n = 33 spheroids pooled across 3 independent experiments; one-way ANOVA/Tukey's). Scale bar, 100 μm.

(D) Representative images of 3D invasion assays of healthy non-cancer-associated fibroblasts and UTSCC47 cells. Images show middle brightfield plane and max-Z projection of confocal stack. Dashed white line outlines spheroid edge. Note that UTSCC74 cells do not co-assemble spheroids with non-cancer-associated fibroblasts and co-invade. Scale bar, 100 μm.

(E) Dot plot showing relative expression of each quantified marker for the phenotypic clusters from transplanted cancer cells.

(F) Relative abundance of phenotypic clusters across the transplants. Note abundance of Sox2-high cluster in UTSCC76 cells, whereas UTSCC74 cells are more abundant in pEMT states and respond to CAFs by increasing AREG-high cells (n = 3 mice [UTSCC74], 4 mice [UTSCC76, UTSCC76+CAF], and 5 mice [UTSCC74+CAF]).

(G) Representative immunofluorescence images and corresponding spatial projections of phenotypic clusters show UTSCC74 response to CAFs and enrichment or AREG-high cells at the tumor-stroma interface. Scale bars, 500 μm.

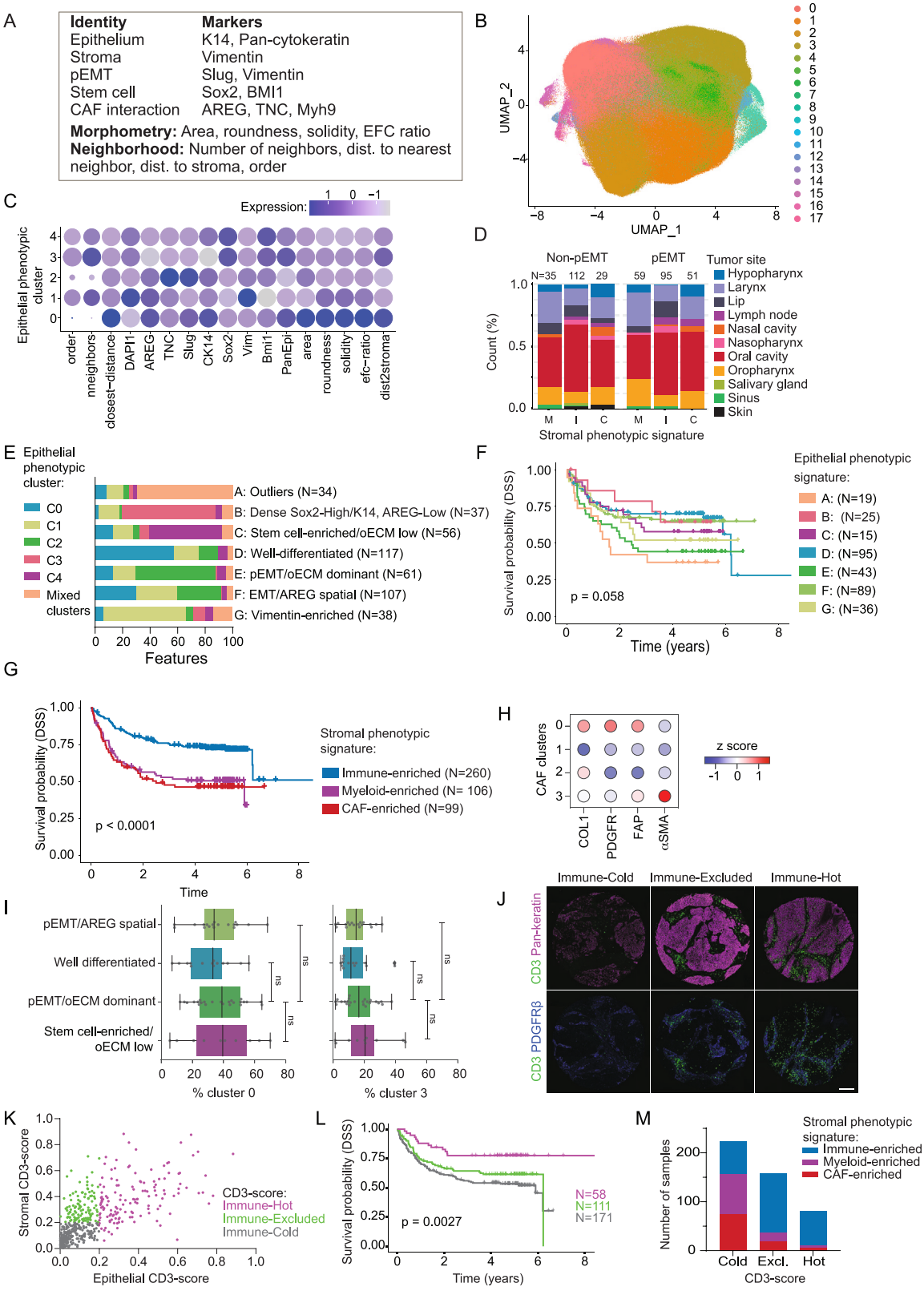

(legend on next page)

Figure S6. Tumor profiling from an independent cohort with additional markers for tumor-stroma crosstalk, related to Figure 6

(A) Markers and parameters used in the epithelial multiplexed immunofluorescence panel of an independent HNSCC patient cohort containing 438 primary tumors.

(B) UMAP plot showing all clustered epithelial cells of the second TMA cohort.

(C) Relative expression levels of each quantified parameter across the five most common epithelial phenotypic clusters.

(D) Distribution of primary tumor sites across the pEMT and non-pEMT epithelial phenotypic signatures grouped according to their stromal signature (M, myeloid-enriched, I, immune-enriched; C, CAF-enriched). HPV+ oropharynx samples removed.

(E) Average distributions of epithelial phenotypic clusters across the seven identified epithelial signatures.

(F) Disease-specific survival (DSS) across the epithelial phenotypic signatures; log-rank test. HPV+ oropharynx samples removed.

(G) Disease-specific survival of all patients in the second TMA cohort stratified by their stromal signature; log-rank test.

(H) Average marker expression for each CAF cluster.

(I) Distribution of the proportions of the most abundant CAF subclusters across epithelial signatures. Each point represents a single patient. No differences in CAF populations are observed (ns, not significant; $p = 0.496$; ANOVA). Minimum-to-maximum box plots show 75th, 50th (median), and 25th percentiles.

(J) Representative images of tumor cores showing distributions of CD3+ T-cells infiltrating into the tumor epithelium and in the stroma. Scale bar, 200 μm.

(K) Quantification of tumor-infiltrating CD3+ T-cells as a proportion of all epithelial cells (epithelial CD3 score) and as a proportion of all stromal cells (stromal CD3 score) in the second TMA patient cohort. Each dot represents one tumor. Colors denote the derivation of global CD3 scores.

(L) Disease-specific survival based on CD3 score in the second TMA cohort; log-rank test. HPV+ oropharynx patients removed. Patients with immune-hot tumor have significantly highest survival.

(M) Distribution of CD3 scores among stromal phenotypic signatures in the second patient cohort.